

1-1-2017

# Diffraction Model of Thermoreflectance Data

Sahida Rahimbhai Kureshi  
*Santa Clara University*

Follow this and additional works at: [http://scholarcommons.scu.edu/eng\\_phd\\_theses](http://scholarcommons.scu.edu/eng_phd_theses)

 Part of the [Mechanical Engineering Commons](#)

---

## Recommended Citation

Kureshi, Sahida Rahimbhai, "Diffraction Model of Thermoreflectance Data" (2017). *Engineering Ph.D. Theses*. 7.  
[http://scholarcommons.scu.edu/eng\\_phd\\_theses/7](http://scholarcommons.scu.edu/eng_phd_theses/7)

This Dissertation is brought to you for free and open access by the Student Scholarship at Scholar Commons. It has been accepted for inclusion in Engineering Ph.D. Theses by an authorized administrator of Scholar Commons. For more information, please contact [rscroggin@scu.edu](mailto:rscroggin@scu.edu).

SANTA CLARA UNIVERSITY

Department of Mechanical Engineering

Date: January 1, 2017

I HEREBY RECOMMEND THAT THE THESIS PREPARED UNDER  
MY SUPERVISISON BY

**Sahida Rahimbhai Kureshi**

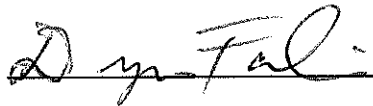
ENTITLED

**DIFFRACTION MODEL OF THERMOREFLECTANCE DATA**

BE ACCEPTED IN PARTIAL FULFILLMENT OF THE  
REQUIREMENTS FOR THE DEGREE

OF

**ENGINEER'S DEGREE IN MECHANICAL ENGINEERING**



Dr. Drazen Fabris, Adviser



Dr. Cary Yang, Reader



Dr. Drazen Fabris, Chair

# **DIFFRACTION MODEL FOR THERMOREFLECTANCE DATA**

By

**Sahida Rahimbhai Kureshi**

Submitted

To

Department of Mechanical Engineering

Santa Clara University

In the requirement of the partial fulfillment of the

**Engineer's Degree in Mechanical Engineering**

## **ABSTRACT**

Diffraction based mathematical model is developed to address the issue of spatial resolution in thermorefectance imaging at the scale of 1 and 10  $\mu\text{m}$ . Thermorefectance imaging provided non-contact temperature measurement at micro and nano scale but the spatial resolution is limited by diffraction. By virtue of this work mathematical model is developed for the analysis of thermorefectance data. In the development of model both the diffraction occurring at sample and substrate is combined to calculate intensity of thermorefectance signal. This model takes into account the effective optical distance, sample width, wavelength, signal phase shift and reflectance intensity. Model shows qualitative and quantitative agreement with experimental data for the two wavelengths under investigation, 470 nm and 535 nm.

# DEDICATION

This dissertation is dedicated to my husband, Rizvan, and our children, Rushan and Rifa. I express my deepest expression of love and appreciation for the encouragement you gave me during this study. You were the strong pillar of my motivation to complete this study. Thanks for your patience and support.

## **ACKNOWLEDGEMENTS**

My deepest gratitude is to my advisor, Dr. Drazen Fabris. I have been amazingly fortunate to have Dr. Fabris as my supervisor. His continuous support and encouragement during my study at Santa Clara University helped me to overcome many crisis situation. I wouldn't imagine this degree to be complete without his motivation and the trust he put on me. I am grateful to him for holding me to a high research standard and enforcing strict validations for each research result, and thus teaching me how to do research. Under his supervision I publish my first peer reviewed article.

I am grateful to Dr. Cary Yang for allowing me to work in his group. I am also thankful to him for encouraging the use of correct grammar and consistent notation in my writings and for carefully reading and commenting on countless revisions of the journal article manuscript.

I would like to acknowledge my fellow researchers Chris Cardenas and Shawn Tokairin to provide experimental data for validation of my model and giving comment on article manuscript.

Most importantly, none of this would have been possible without the love and patience of my family. My immediate family to whom this dissertation is dedicated to, has been a constant source of love, concern, support and strength all these years. I would like to express my heart-felt gratitude to my family. I must give special thanks to my parents at back home in India who has aided and encouraged me throughout my life and in this endeavor.

Finally, I appreciate the financial support from Dean of Engineering and Packard fellowship.

## TABLE OF CONTENT

1. Introduction	1
1.1 Introduction	1
1.2 Thermoreflectance Method	6
1.3 Diffraction	12
2. Mathematical Model	
2.1 Diffraction Theory	15
2.2 Diffraction by slit	18
2.3 Diffraction by strip	20
2.4 Mathematical Model	20
3. Results and Analysis	23
4. Conclusion and Future work	30
References	31
Appendices	
A.1 Thermoreflectance Experimental set-up	34
A.2 MATLAB code	36

## LIST OF TABLES

Table 1.1	Summary of popular high-resolution thermal measurement techniques in micrometer-nanometer range	1
Table 3.1	Summary of Fitting parameters	25
Table A.1	Spectral characteristics of LEDs	33

## LIST OF FIGURES

Fig. 1.1	Gold line sample used for electrical interconnect testing and thermoreflectance testing in prior work [7,14] (a) Top view of sample (b) section-view of sample (c) microscopy obtained reflectance intensity image under LED wavelength of 535 nm. Section a-a captures a region of the gold line structure at 10 micron wide whereas in section b-b the width is 1 micron	13
Fig. 2.1	Diffraction field for Rayleigh-Sommerfeld diffraction Integral	16
Fig. 2.2	Effect of distance z on diffracted field intensity (a) slit (b) strip for different image plane distances from the sample	19
Fig. 2.3	Mathematical model set-up composed of reflection from the sample and substrate based on two simple diffraction model (a) The diffracted field for the gold line, where gold line is treated as slit (b) The diffracted field for the substrate, where gold line is treated as a strip blocking the light reflected from the substrate.	21
Fig. 3.1	Plot of experimental data and model for 10 $\mu\text{m}$ wide gold interconnect for (a.) $\lambda = 535\text{nm}$ at section a-a of Fig. 1.1 (c) and (b.) $\lambda = 470\text{ nm}$ at section a-a of Fi. 1.1 (c)	26
Fig. 3.2	Plot of experimental data and model for 1 $\mu\text{m}$ wide gold interconnect for (a) $\lambda = 535\text{ nm}$ at Section b-b of Fig. 1.1(c) and (b) $\lambda = 470\text{ nm}$ at Section b-b of Fig. 1.1(c)	28
Fig. A.1	Schematic of Thermoreflectance temperature measurement experimental set-up	35



# 1. INTRODUCTION

## 1.1 Introduction:

Miniaturization has become synonyms of semiconductor devices in the current era. The size of electronic devices and line in current ICs has shrunk to 24nm [1]. The reduced size of devices out perform in terms of switching speed and fabrication cost. However, the shrunk size of electronic devices gives new challenges to heat management design. The main barrier in the development of micro and nano scale devices is the resulting large current density and local heating. In the last twenty years it has become more challenging for designers to understand the heat transfer and thermal characterization at micro and nano scale due to small size of electronic devices. Temperature mapping at micro and nano scale is very important for safe and reliable operation of small scale electronic devices [2, 3]. With electronic devices in the range of size few nano meters to micrometers the conventional methods of temperature measurement like Infrared radiation thermometry and the micro-Raman methods is no more useful.

Various methods of temperature measurement on the scale of current electronic and optoelectronic devices are surveyed by Christofferson et al. [4] and Wenjun et al. [5].

Table 1.1 present the summary of these methods:

**Table 1.1: Summary of popular high-resolution thermal measurement techniques in micrometer-nanometer range**

Method	Principle	Resolution			Imaging ?
		Spatial ( $\mu\text{m}$ )	Temperature (K)	Response time (s)	
Micro-thermocouple	Seebeck effect	50	0.01 0.02 (if blackbody )	5 m 10 $\mu\text{m}$ (single point)	No

Infrared thermography	Planck blackbody emission	3-10	-1 K	-0.5 m (image)	Yes
Liquid crystal thermography	Crystal phase transitions (change color)	2-5	0.5 (near phase transition)	3 m	Yes
Thermo-reflectance	Temperature dependence of reflection	0.3-0.5	0.01	0.006-0.1 $\mu\text{m}$	Yes
Scanning Thermal microscopy (SThM)	Atomic force microscope with thermocouple or Pt thermistor tip	0.05 (surface morphology)	0.1	10-100 $\mu\text{m}$	Scan
Fluorescence thermography	Temperature dependence of quantum efficiency	0.3	0.01	200 $\mu\text{m}$	Scan
Optical interferometry	Thermal expansion, Michelson type	0.5	0.0001 (1 fm)	0.006-0.1 $\mu\text{m}$	Scan
Micro-Raman	Shift in Raman frequency or ratio of Stokes/anti-Stokes amplitudes	0.5	1	1 $\mu\text{m}$	Scan
Near field probe (NSOM)	Use near field to improve optical resolution	0.05	0.1-1 (S/N dependent)	0.1-10 $\mu\text{m}$	Scan
Built-in temperature sensors	Fabricate a thermal sensor integrated into the device	100s	0.0002-0.01	1 $\mu\text{m}$	No

All the methods summarized in Table 1.1 can be broadly classified into two categories: (1.) contact measurement and (2.) non-contact measurement. Following are some advantages offered by Non-contact methods over contact methods:

- (i) Fast – allowing more measurements to take and therefore it is more convenient for large data acquisition (Temperature mapping)
- (ii) Measurements can be taken of object surrounded by hazardous material
- (iii) Non-destructive measurement

However, all the non-contact measurement methods are limited by onset of diffraction.

The most promising techniques regarding spatial resolution are those involving contact probes [6], which are usually limited to the measurement of surface temperatures. In integrated circuits, mainly the heat is generated due to joule heating in metal thin films and contacts, those are often buried under a few hundreds of nanometers or several micrometers of encapsulation dielectric. Therefore, the use of thermocouples and in-built sensors, integrated within the circuit is good option. After calibration, they deliver high precision and high sensitivity temperature measurements but provide no spatial information [6]. Moreover, due to the presence of interfaces, strong temperature gradients can exist in integrated circuits, leading to discrepancies between the temperature of the active region and that measured by the sensor.

Infrared (IR) thermometry is one of the most widely used technique for temperature measurements of electronic devices, particularly ICs [4]. IR thermometry is based on determining the spatial distribution of IR thermal radiation emitted from the surface of a solid [4]. Based on Planck's law of blackbody radiation, the maximum spectral power density of an ideal blackbody at thermal equilibrium will shift to lower wavelengths with increasing temperature. Since, in practice the surface of a device under study is not a blackbody and reflects some of the incident radiation, the blackbody law must be scaled by a material dependent factor known as the emissivity. Emissivity depends on the surface property and geometry, wavelength and temperature of the object, and must be known for each surface to obtain an accurate thermal profile. Silicon is largely transparent to near IR radiation, making IR thermography a valuable tool for thermal mapping of IC backplanes and hot spots. The thermal resolution of IR cameras can be 10-20 mK [4], but their spatial resolution is mainly determined by the diffraction limit for the range of wavelengths to which the detector is sensitive. The most sensitive IR cameras work at 3  $\mu\text{m}$  wavelength [4], which is not suited to the length scales of many

modern electronic and optoelectronic devices. Apart from the sub-optimal spatial resolution of IR thermography, other drawbacks include inaccuracy due to the attenuation of radiation between the target and the detector, uncertainty in the emissivity of the device surface and background radiation [5]. Furthermore, material likes most metals with high reflectivity and the low emissivity limits the application of IR thermography. Liquid crystal thermography (LCT) and fluorescence microthermography (FMT) are semi-invasive thin coating methods. In the LCT technique [4, 5], the surface of the device under study is covered with a thin layer of liquid crystal and illuminated with white light. At different temperatures, the liquid crystal layer reflects different wavelengths of this incident light. The theoretical limit for the resolution of the method was estimated to be 25  $\mu\text{m}$  spatially and 0.1 K in temperature [5]. To improve the spatial resolution of the method, the nematic–isotropic phase transition of liquid crystal which occurs at the clearing point of the crystal is used [5]. It is stated by Wenjun & Yang [5], and the reference there in, “Below clearing point the liquid crystal is in the nematic phase which scatters light and rotates the plane of polarization of the light and appears bright under a polarizing microscope. Above clearing point, where the liquid crystal is in the isotropic phase, the plane of polarized light does not change and the image field appears dark. Taking advantage of the nematic–isotropic phase transition has given the LCT method a spatial resolution of 2–4  $\mu\text{m}$ ”. Due to semi-invasive nature of LCT technique the thermal conductivity and heat capacity of the liquid crystal coating can affect the device under test. In addition, the uniformity and thickness of the liquid crystal layer are important factors in the accuracy and resolution of the technique [4]. Fluorescent microthermography (FMT) [4, 5] utilizes the temperature-dependent quantum efficiency of photoluminescent rare earth dyes. As mentioned by J. Christofferson *et al* [4], in FCT technique, “the sample surface is coated with a thin film of such dyes and is then illuminated by ultraviolet (UV) light”. FMT can be used for thermal imaging of electronic and bio sensing devices as well as hot spot detection and thermal mapping of ICs. A spatial resolution of 0.3  $\mu\text{m}$  and a thermal resolution of 1 mK have been reported for FMT [4], although sample preparation and optical system design require special

consideration. Photon shot noise, UV bleaching, film dilution and film preparation can have a significant impact on the quality of FMT thermal images.

Using micro-thermocouples as inexpensive point measurement contact probes can provide accurate temperature readings with a thermal resolution of 0.01 K [5]. However, as stated by Wenjun & Yang [5], the large size of the thermocouple wires ( $\sim 25\text{-}50\ \mu\text{m}$  diameter) results in a poor spatial resolution. In addition, due to difficulties in maintaining good thermal contact between the micro thermocouple junction and the surface of a device results in faulty readings. Finally, as point-based measurement tools, micro-thermocouples cannot be used for imaging without implementing complicated translation stages [5]. Scanning Thermal Microscopy (S<sub>Th</sub>M) is a contact thermometry technique with very high spatial resolution. S<sub>Th</sub>M utilizes the mechanism behind atomic force microscopy (AFM) and scanning tunneling microscopy (STM). The S<sub>Th</sub>M probe consists of a thermocouple fabricated on the tip of an AFM cantilever [6]. When the probe is scanned in contact mode over the surface of a sample, localized heat transfer between the sample surface and the probe tip leads to a change in the tip temperature that is measured by the thermocouple. In this way, both the tip-sample heat transfer across the entire surface and the sample topography can be obtained simultaneously with sub-micrometre spatial resolution ( $\sim 0.05\ \mu\text{m}$ ) and a thermal resolution of 0.1K [4]. However, the roughness of the sample surface can cause variations in the tip-surface thermal contact, leading to noise in the thermal signal. Furthermore, the S<sub>Th</sub>M experimental setup is complicated and expensive, and data acquisition can be time-consuming due to the required scanning methods [5]. A major limitation of S<sub>Th</sub>M is the liquid meniscus that forms between the tip and the sample, which is intrinsic to contact measurements done in atmosphere and limits the resolution of the technique. Finally, S<sub>Th</sub>M cannot be used easily on light emitting surfaces of optoelectronic devices such as vertical cavity surface emitting lasers (VCSELs), because the light is absorbed by the S<sub>Th</sub>M thermocouple and causes errors in temperature measurement [6]. Raman spectroscopy is an optical measurement technique that is well suited for temperature measurements in microelectronic devices, especially made from silicon, due to its strong scattering cross-section [5]. The Raman technique provides spatial resolutions on the order of 1  $\mu\text{m}$  or

smaller considering far field diffraction limited optics [5]. In addition to the above-mentioned techniques, other methods of thermography include acoustic thermography, near-field scanning optical microscopy (NSOM) adapted for temperature measurement, laser interferometry and thermoreflectance microscopy. This last thermography method is the focus of this research work and will be discussed in detail in the next sections.

### **1.1 Thermoreflectance Method:**

Thermoreflectance (TR) temperature measurement belongs to the class of non-contact temperature measurements and uses an LED or filtered white light source and a CCD to acquire images. TR techniques offers direct access to the active areas under the transparent encapsulation layers. In the visible or near UV range, excellent spatial resolutions can be reached. It has been shown that the thermal and spatial resolutions of CCD-based thermoreflectance can be as low as 10 mK and 250 nm, respectively [6], but the fundamental temperature limit has not been found yet. The major advantage of TR microscopy is: relatively short data acquisition times compared with other techniques and its suitability to a wide range of materials including metals and light emitting surfaces. Thermoreflectance temperature measurement is based on the principle that a change in temperature of a given material produces a small change in the spectral reflectivity of the material's surface [6-9]. This small change can be linearized over a range of temperature. The linearized response of the normal reflectance with respect to the temperature of a sample allows the following approximation for the derivative of normal reflectance [8]

$$\frac{\partial \rho_n}{\partial T} \approx \frac{\rho_n(T) - \rho_n(T_0)}{T - T_0} \quad (1)$$

The normal reflectance intensity at a given temperature,  $I_n ( T )$ , can be calculated from the normal reflectance,  $\rho_n(T)$  and incoming illumination intensity  $I_0$

$$I_n (T) = \rho_n (T) \cdot I_0 \quad (2)$$

The spectral thermoreflectance (TR) coefficient  $\kappa$  is defined by the normalization of the slope as a function of temperature with the reference quantity [8]

$$\kappa = \frac{1}{\rho_n(T_0)} \frac{\partial \rho_n}{\partial T} = \frac{1}{I_n(T_0)} \frac{\partial I_n}{\partial T} \quad (3)$$

During the experiment, it is necessary to calibrate the system and obtain the thermoreflectance coefficient for the specific sample. Following the calibration, one can determine the temperature difference developed during heating through rearrangement of the governing relationship with a measurement of the relative reflectance.

$$\Delta T = (T - T_0) = \frac{1}{\kappa} \left( \frac{I_n(T) - I_n(T_0)}{I_n(T_0)} \right) \quad (4)$$

The thermoreflectance coefficient is a material and surface property that depends on the illumination wavelength, temperature, microscope, material surface characteristics and in some cases also on the material processing [9]. For most metals and semiconductor materials of interest the value of the thermo-reflectance coefficient ( $\kappa$ ) will be in the order of  $10^{-2}$  to  $10^{-5} \text{ K}^{-1}$  [6-10].  $\kappa(\lambda)$  can vary sharply within the spectral region of interest particularly in the visible spectrum, and therefore the choice of illumination wavelength determines not only the spatial resolution of the technique but also the sensitivity of method. It is essential to choose a wavelength for which the change in reflectivity is highest for given change in temperature and reflectivity has minimum value [10]. In addition, electronic and optoelectronic device analyzed with TR microscopy generally have layered structures that strongly modifies the TR coefficient. The protection layer of integrated circuits is made of dielectric material which is transparent to visible light. The optical interference which occurs in these layers strongly modifies the reflectivity and can

even forbid thermorefectance measurements at some wavelengths. For each series of circuits, it is therefore necessary to determine the illumination wavelengths for which thermorefectance will deliver optimal signals [10, 11]. As stated in [10], one way to calibrate thermorefectance for range of spectrum is to use different LEDs as illumination sources, and measure the photothermal response at each LED wavelength. This has been demonstrated on a 45 nm thick NiCr oxide resistor deposited on a GaAs substrate with 1.5 $\mu$ m thick Au Ohmic contacts and blanked coated with a Si<sub>3</sub>N<sub>4</sub> passivation layer [10]. It is observed by G. Tessier *et al* [10], that red LEDs ( $\lambda = 615$  and 660 nm) exhibited low response for both bare and passivated Au, while an orange LED ( $\lambda = 598$  nm), was shown to be suitable for thermal imaging of passivated NiCr and Au. Further they found “green illumination ( $\lambda = 511$  nm) gave a large signal for Si<sub>3</sub>N<sub>4</sub>-coated GaAs and a small signal for passivated Au”. Therefore, it is possible to measure the thermal behavior of a selected material within a complex structure by careful choice of the illumination wavelength. This method is very time consuming and therefore subject to drifts. To improve the calibration method G. Tessier *et al.* [11] has developed a CCD camera-based thermorefectance microscope coupled to a grating which disperses white light directly onto the CCD. This instrument gives the complete spectra of the reflection coefficient and its temperature dependence, reflectivity and the ratio of change in reflectivity with respect to change in temperature can be measured on one or several materials with only one acquisition. The optimal wavelength for thermorefectance measurements can therefore be measured within minutes on any sample. A model considering multiple reflections and the thermal expansion of the encapsulation layer has been also developed in this work [11] to explain the spectra and variation of TR coefficient for given spectra on encapsulated circuits. This model can be used to predict qualitatively the optimal working wavelength. Alternatively, Peltier element control of the whole package temperature in order to obtain calibration coefficients simultaneously on several materials visible on the surface of the circuit is proposed [12]. Under high magnifications, movements associated with thermal expansion are corrected using a piezo electric displacement and a software image shift. In this work [12] the temperature obtained by thermorefectance have been compared with those obtained by two sensors, a thermistor

and a diode junction. The agreement with thermorefectance and simulation is very good, with a standard deviation of the order of 2.3%. As it is mentioned in [4-6], while thermorefectance is a very sensitive and high resolution tool for temperature mapping, its precision is still two orders of magnitude lower than its thermal resolution, mainly due to the complexity of calibration procedures. Efforts remain to be made to make precision and temperature resolution comparable. Noninvasive method for thermorefectance coefficient calibration ideally suited for in-chamber, and thus high temperature has been developed in [13]. Thermorefectance coefficients for three commonly encountered metals in electronic devices: gold, platinum, and aluminum is explained in this work [13]. The effect of passivation on these metals is also examined, and it is demonstrated the signal to noise ratio of a thermorefectance measurement can be improved with informed selection of the dielectric layer thickness. For gold, the behavior of TR coefficient is analyzed under 455, 470, and 530 nm illumination in the measurement chamber from room temperature to 500 K. For the given  $\Delta T$  inside the thermostat, bare gold illuminated at 530 nm has the highest thermorefectance response, followed by 470 nm and then 455 nm. Further, the reflectivity signal is significantly enhanced in the passivated region at 530 nm, but is slightly diminished at 470 nm with almost no change at 455 nm [13], relative to bare gold metal. The average rate of change in the TR coefficient of bare gold metal is measured of  $0.30 \times 10^{-4}$  per 100K temperature [13].

Frequency-Domain measurement techniques, lock-in method of thermorefectance microscopy has proven effective in obtaining thermal images of active electronic and optoelectronic devices with submicron spatial resolution and 10-50mK temperature resolution [6]. Thermorefectance systems that use a lock-in method capture the steady state thermal signal but provide limited information about the thermal transient.

However, it is often desirable to observe how devices thermally evolve in time. Due to the size of typical electronic and optoelectronic devices, thermal effects can occur on a millisecond or microsecond time scale or faster [6]. Thermorefectance methods based on time domain analysis can characterize fast transient heating effects such as the thermal rise time by reconstructing the time varying reflectance signal. Burzo *et al* [14] has demonstrated first experimental system capable of noninvasively and nondestructively

scanning the transient surface temperature of pulsed microelectronic devices with submicron spatial and sub-microsecond temporal resolutions. Burzo *et al* [14] have used the experimental set-up to scan the active area of typical MOSFET devices of differing gate widths and lengths. Both quasi steady-state and transient temperature measurement results are obtained with overall random uncertainty of the results to be less than 13% [14]. In order to partially overcome the slow frame rates associated with CCDs, Maize *et al* [15] have used a pulsed LED and a CCD camera to acquire transient thermal images almost 100 times faster than single point TTR, without the need for a laser and scanning translation stage. Their technique utilizes a pulsed boxcar averaging scheme in which the boxcar average is combined with a short duration LED pulse ( $\sim 10$  ns) synchronized with device excitation. For each exposure of the CCD, there is one LED pulse, effectively reducing the camera exposure to the time duration of the LED pulse width. For the next integration period of the CCD, the phase between the LED pulse and the device excitation is advanced by a small, known amount, and the in-between data points are filled in by combining multiple boxcar averages. By stepping the light pulse in regular increments, the CCD thus records the full thermal transient of the device with time resolution limited by the pulse width. This method has been used to demonstrate transient thermal imaging of a micro-heater with millisecond and microsecond time resolution, comparing rapid heat diffusion in the device metal to slower diffusion into the substrate [15]. An example of transient thermal imaging on a test chip is studied in [16]. This work [16] discusses the relationship of spatial resolution and time resolution considering the ‘time constant’ component of chip. Spatial resolution for thermoreflectance is limited by the diffraction of the illuminating light, time resolution is limited by the high speed electrical signal management, and temperature resolution is limited by the signal-to-noise ratio [16]. In the current work issue of spatial resolution is addressed and detail explanation is given in next sections.

Application of frequency-domain thermoreflectance is extended to the characterization of thin metals films on low thermal diffusivity substrates [17]. It is seen, how a single noncontact measurement can yield both the thickness and thermal conductivity of a thin metal film with high accuracy. Results are presented from

measurements of gold and aluminum films 20–100 nm thick on fused silica substrate. The thickness measurements are verified independently with atomic force microscope cross sections, and the thermal conductivity measurements are verified through electrical conductivity measurements via the Wiedemann–Franz law. The thermoreflectance thermal conductivity values were in good agreement with the Wiedemann–Franz results for all the films at least 30 nm thick, indicating that presented method can be used to estimate electrical conductivity along with thermal conductivity for sufficiently thick films.

Thermoreflectance measurement system can provide exact thermal information to identify defects in a device that are hardly perceptible with the IR thermography system and the conventional widefield microscope system [18]. By determining the thermoreflectance calibration coefficient experimentally, quantitative temperature distribution of polysilicon micro-resistors was obtained in [18]. Using their proposed thermoreflectance measurement system on a polysilicon micro-resistor, a high thermal resolution of up to ~13 mK was achieved in 50,000 iterations by using a high bit-depth CCD camera, and a high spatial resolution of ~670 nm was realized with a 100× (0.5 NA) objective lens and visible light source (635.9 nm). The obtained thermoreflectance calibration coefficient of polysilicon was  $-1.71 \times 10^{-3}$  with illumination light at  $\lambda=635.9$  nm and a 20× (0.42 NA) objective lens [18].

The application of thermoreflectance CCD imaging in power microelectronics is demonstrated in [19]. Thermoreflectance imaging with submicrometer spatial resolution and 50 mK temperature was used to study self-heating temperature distribution in LDMOS silicon power transistor arrays under dc operation. Thermoreflectance images revealed highly nonuniform spatial self-heating distribution in the active power arrays.

The major drawback of Thermoreflectance measurement technique are: sensitivity of method to illumination wavelength and the diffraction limited spatial resolution. The problem of diffraction is discussed by Grauby et al., but no suggestions was given to handle this issue [20]. Recently A. Ziabari et. al. [21], came up with idea of numerical simulation and analytical model to address the issue of diffraction in thermoreflectance imaging. They have developed analytical model based on Bessel's function and found thermoreflectance coefficient for sample and

substrate. Further did simulation using ANSYS APDL and then combine results with analytical model to obtain final temperature profile.

## **1.2 Diffraction:**

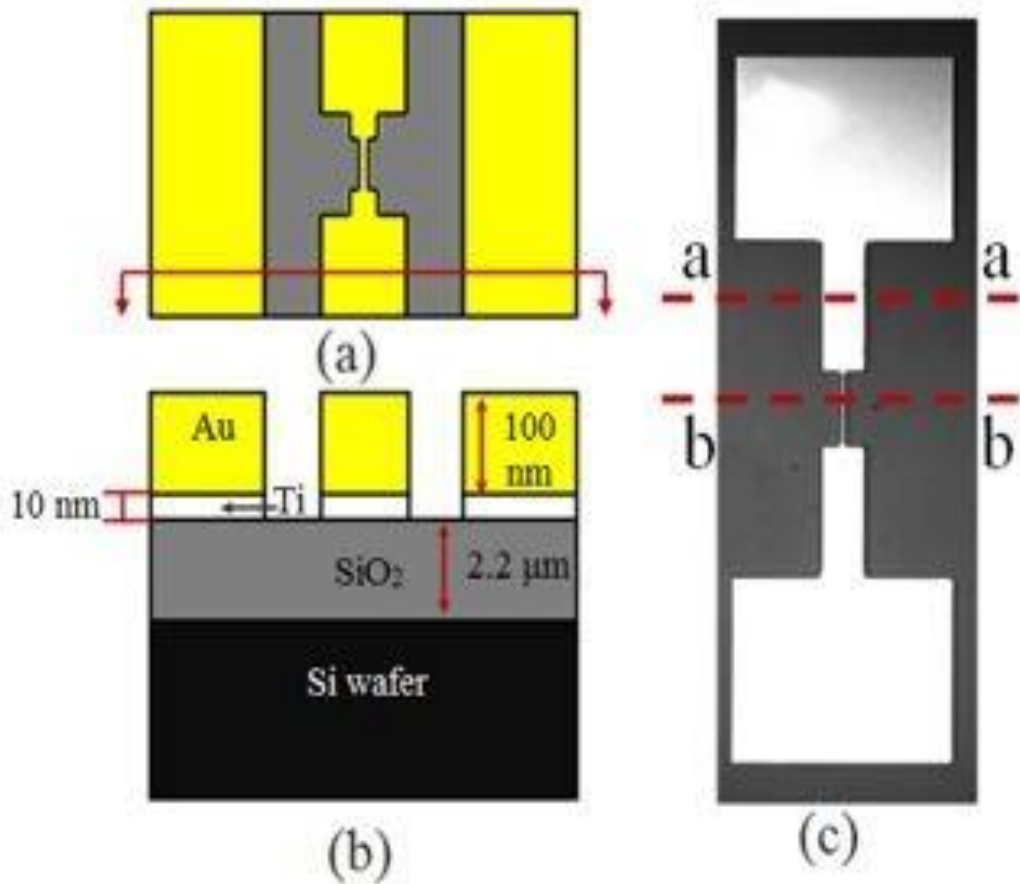
Diffraction effects are consequence of the wave nature of light. Diffraction means any deviation of light rays from rectilinear that cannot be interpreted as reflection or refraction [22], was long back first reported by Grimaldi in 1665. When some obstruction is present in the path of light wave, resulting pattern on the other side of obstacle can be explained with diffraction theory. The obstacle need not to be opaque but if causes local variations in the amplitude or phase of the wavefront of light such effects are observed. Because the diffraction cause the blurring at edges of any optical images, diffraction phenomenon leads to fundamental limitation in instrument resolution. Rayleigh criterion along with lens maker equation estimates the limit of resolution and it is approximately half of wavelength of light reflected from surface. Due to this resolution limitation set by diffraction abundant work is done to understand theory of diffraction and thereby to improve the resolution.

As mentioned in section 1.2 non-contact thermal measurements has spatial resolution limitation due to diffraction. Infrared Thermography has spatial resolution in the range of 3-10  $\mu\text{m}$  due to use of infrared range light source in imaging. Thermoreflectance Imaging temperature measurement also has spatial resolution limit due to diffraction. In the prior work, thermoreflectance was used to measure the temperature of thin gold films that modeled electrical interconnects. The modeled interconnects were 1 to 10  $\mu\text{m}$  in width and tens of  $\mu\text{m}$  long. In this work a mathematical model is developed for better analysis of the thermo-reflectance experimental data. The main purpose of this work is to understand the impact of diffraction and the parameters that govern the signal.

The model developed in the course of this thesis is based on Rayleigh-Sommerfeld diffraction formula that is the reformulation of Kirchoff's diffraction formula with Dirichlet green's function (i.e., one that vanishes on the boundary surface). A one-dimensional Fresnel diffraction formula is used to estimate diffracted field from the observed sample and the background. The mathematical model further takes into account

the incoherent nature of the illumination source by averaging over the wavelengths of the light source. The remaining unknown parameters of the experiments are treated as free parameters and are determined by a comparison to the experimental data. Detailed explanation about diffraction theory and the mathematical model are discussed in Chapter - 2.

Experimental data used here for comparison are taken from the Master's thesis of Cardenas [9] and briefly summarized here. The thermoreflectance technique was used to measure temperature and determine thermal contact resistance for gold thin film structures used as model electrical interconnects [8, 9]. The observed sample consists of the gold thin film interconnects as seen in Fig. 1.1.



The test interconnect consists of two gold pads, thin film leads and a narrow test line connecting the two leads [23, 24]. The gold film is deposited on an amorphous SiO<sub>2</sub> substrate grown on a silicon wafer. There is thin adhesion layer of titanium between gold and SiO<sub>2</sub>. This

technique was extended to analyzing thermoreflectance data from 150 nm wide carbon nanofibers (CNFs) undergoing current stressing [25].

The thermoreflectance experiment was performed in two stages: *i*) Calibration: to obtain the thermoreflectance coefficient the entire sample was uniformly heated using a heater and the normal reflectance intensity was measured by using a microscope and CCD; and *ii*) Temperature Measurement: the TR coefficient was then used to measure temperature distribution of the thin gold structure undergoing Joule heating. In prior experiments, the calibrated TR coefficient shows good experiment with the work of Beran [26]. However, the calibrated TR coefficients under the illumination wavelengths of 470 and 530 nm yielding different values [8]. Whereas a temperature measurement from Joule heating was possible at 530 nm, the 470 nm data for the small interconnect lines were strongly influenced by diffraction. In both cases, but more pronounced at 470 nm, the size of the measurement sample affects the quality of the result. The combined effects of vibration and diffraction cause spatial averaging and convolution (blurring) and lead to mixing of the reflectance intensity of the gold film and substrate. The amount of diffraction depends upon the wavelength, the size of the sample, and the interaction with background. When measuring on the gold pads (10  $\mu\text{m}$  wide) the thermal profiles obtained from the experiment for the wavelengths 470 and 530 nm match. The disagreement in the calibration and the measurement signal exists over the narrow interconnect (1  $\mu\text{m}$  wide) samples motivates the development of a diffraction based model. We are not aware of any previous work that has investigated methods to use thermoreflectance on very narrow lines where diffraction has taken place.

The present work develops a model to characterize the diffraction, based on the size of the sample, the wavelength of the illumination, the phase shift of the signal from the background, strength of the reflectance, and the apparent distance of the image. From fitting the model with the experimental data the unknown parameters of the experiments are quantified. The parameters are optical distance between the specimen and the CCD, and the phase shift between the signals resulting from the difference in the thickness of the gold line and the substrate. Results are discussed in detail in Chapter-3 of thesis.

## **2. MATHEMATICAL MODEL**

### **2.1 Diffraction Theory:**

Diffraction is defined by Sommerfeld as any deviation of light from rectilinear path that cannot be interpreted as reflection or refraction [27]. But before that there is fascinating history associated with the discovery and explanation of diffraction effect. The first accurate description of this phenomenon was given by Grimaldi in 1665 in his book. Then in 1678 Huygens expressed the principle that if each point on the wavefront of disturbance were considered to be a new source of a “secondary” spherical disturbance, then the wavefront at a later instant could be found by constructing the “envelope” of the secondary wavelets. Then there was no significant progress on further understanding this phenomenon during 18<sup>th</sup> century. In 1804, Young introduced the concept of “interference” and there by strengthened the wave theory of light. In 1818, Fresnel first time calculated distribution of light in diffraction patterns by combining Huygens and Young’s explanation and making some arbitrary assumptions. After the Maxwell’s discovery of light as an electromagnetic wave in 1860, in 1882 the ideas of Huygens and Fresnel were put on a firmer mathematical formulation by Kirchhoff, who successfully showed that phase and amplitudes described for secondary wavelet by Fresnel is indeed logical sequence of wave nature of light. However two main assumption on boundary conditions made by Kirchhoff was later proved inconsistent by Poincare in 1892 and Sommerfeld in 1894. And therefore the Kirchhoff’s theory is known as first approximation of diffraction theory. The Kirchhoff’s theory then modified by Sommerfeld by eliminating one of the inconsistent assumption regarding the light amplitude at the boundary. Rayleigh Sommerfeld used theory of Green’s Function. In the development of the mathematical model for the thermorefectance data Rayleigh-Sommerfeld theory is used.

The basic diffraction problem requires finding a solution to the Helmholtz equation for propagating wave encountering partial obscuring planar screen [27, 28]. The Helmholtz equation is

$$(\nabla^2 + k^2)E(\mathbf{r}) = 0 \quad (1)$$

where  $k = 2\pi/\lambda$ , the wave number and  $E$  is scalar field.

The boundary condition imposed on the solution to this differential equation is the effect of a diffracting screen in the  $z = 0$  plane (Fig. 2.1).

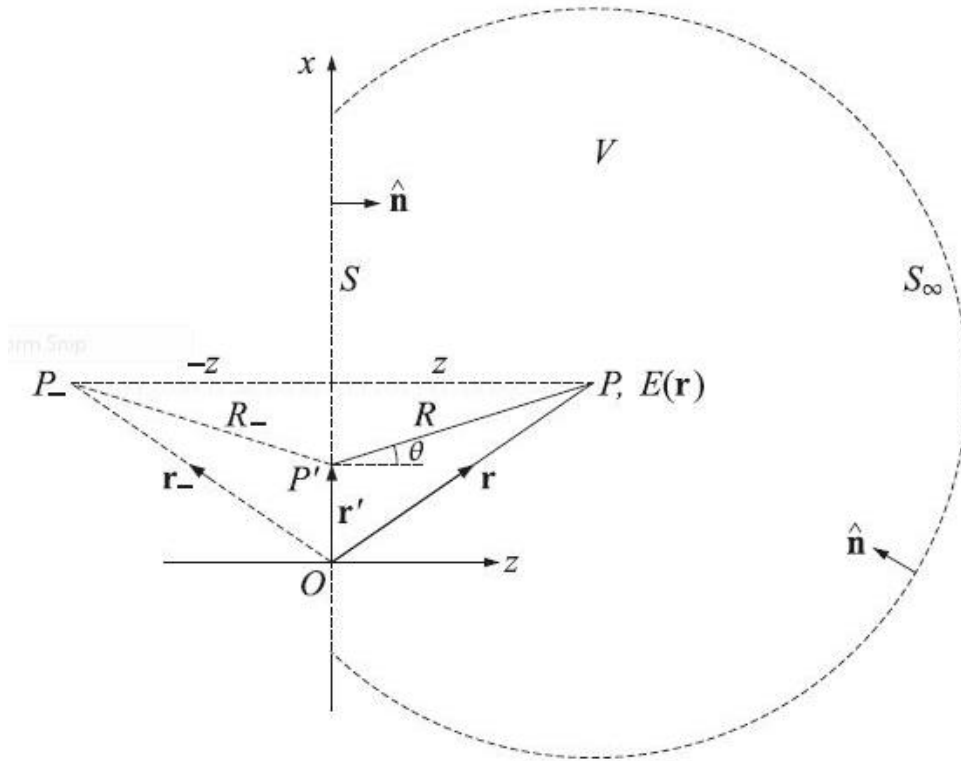


**Fig. 2.1: Diffraction field for Rayleigh-Sommerfeld diffraction Integral**

The Rayleigh-Sommerfeld diffraction integral is given as [29]:

$$E(\mathbf{r}) \iint = 2 \iint_S E(\mathbf{r}_0) \frac{\partial G}{\partial z} dS \quad (2)$$

where  $G$  is the Green's function for the Helmholtz equation.

$$G(r - r_0) = \frac{e^{-jk|r-r_0|}}{4\pi|r-r_0|} \quad \text{or} \quad G(r_{01}) = \frac{e^{-jkR}}{4\pi R} \quad \text{and} \quad (3)$$

$$\left. \frac{\partial G}{\partial z} \right|_{z=0} = \frac{z}{R} \left( jk + \frac{1}{R} \right) \frac{e^{-jkR}}{4\pi R} \quad (4)$$

Substituting value of indicated derivative in equation (2)

$$E(r) = \iint_S E(r_0) \frac{2z}{R} \left( jk + \frac{1}{R} \right) \frac{e^{-jkR}}{4\pi R} dS \quad (5)$$

$$\text{In this equation } R = |r - r_0| = \sqrt{(x - x_0)^2 + (y - y_0)^2 + z^2} \quad (6)$$

Now if we assume that diffracting aperture has dimension 'a' so that  $x_0^2 + y_0^2 \ll a^2$  and further if we assume that  $z$  is large enough that Fresnel number ( $N_f$ ) =  $\frac{a^2}{\lambda z}$  is small enough then equation (5) simplifies to

$$E(x, y, z) = \frac{jk}{2\pi z} e^{-jkz} \iint E(x_0, y_0, 0) e^{-jk|(x-x_0)+(y-y_0)|^2/2z} dx_0 dy_0 \quad (7)$$

The above mentioned approximation is called Fresnel approximation.

In the special case when the aperture field  $E(x_0, y_0, 0)$  depends only one transverse coordinate, say,  $E(x_0, 0)$  the dependence of equation (7) on the  $y$  direction can be integrated out using the integral

$$\sqrt{\frac{jk}{2\pi z}} \int_{-\infty}^{\infty} e^{-jk(y-y_0)^2/2z} dy_0 = 1 \quad (8)$$

and we obtain the following one-dimensional Fresnel formula:

$$E(x, z) = \sqrt{\frac{jk}{2\pi z}} e^{-jkz} \int_{-\infty}^{\infty} E(x_0, 0) e^{-jk(x-x_0)^2/2z} dx_0 \quad (9)$$

## 2.2 Diffraction by Single slit:

The incident field is uniform plane wave,  $E_{inc}(x, z) = E_0 \exp(-jkz)$ , whose value on slit is  $(x_0, 0) = E_0$ .

The diffracted field at distance 'z' from equation (9)

$$E(x, z) = \frac{\sqrt{jk}}{2\pi z} e^{-jkz} \int_{-\infty}^{\infty} E(x_0, 0) \exp\left(-\frac{jk(x-x_0)^2}{2z}\right) dx_0$$

$$= E_0 \frac{\sqrt{jk}}{2\pi z} e^{-jkz} \int_{-a}^a \exp\left(-\frac{jk(x-x_0)^2}{2z}\right) dx_0 \quad (10)$$

where 'a' is the half-width of the slit. The integral can be reduced to Fresnel Integral by changing variable as follows:

$$\sqrt{\frac{k}{2z}}(x-x_0) = \sqrt{\frac{\pi}{2}}u \quad \& \quad v_{\pm} = \sqrt{\frac{k}{\pi z}}(\pm a - x) \quad (11)$$

With this substitution equation (10) reduces to

$$\frac{\sqrt{jk}}{2\pi z} \int_{-a}^a \exp\left(-\frac{jk(x-x_0)^2}{2z}\right) dx_0 = \sqrt{\frac{j}{2}} \int_{v_-}^{v_+} \exp\left(-\frac{j\pi u^2}{2}\right) du$$

$$= \frac{F(v_+) - F(v_-)}{1-j} \quad (12)$$

Thus  $E(x, z) = \exp(-jkz) D(x, z)$ ,

where,

$$D = \frac{F(v_+) - F(v_-)}{1 - j} \quad (13)$$

$$\text{Intensity } (I) = E \times E^* \quad (14)$$

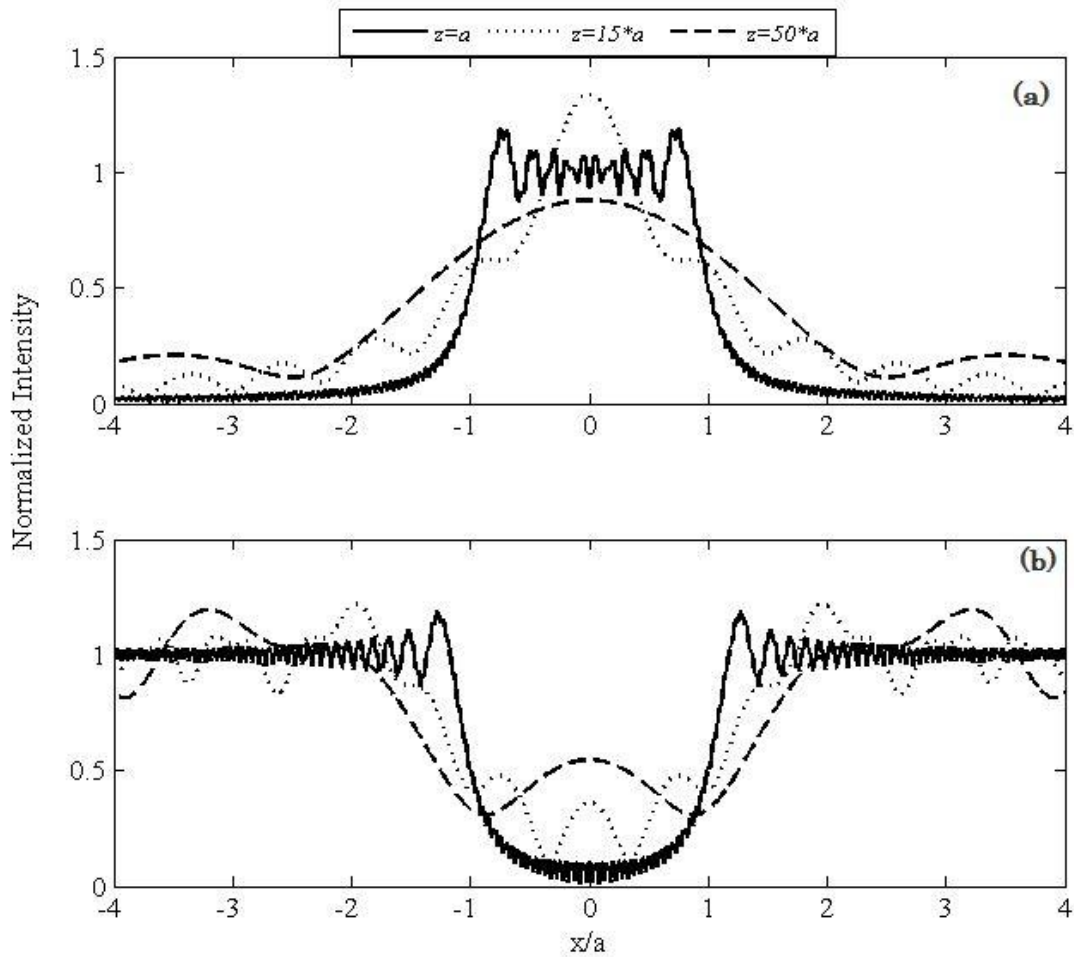


**Figure 2.2 Effect of distance  $z$  on diffracted field intensity (a) slit (b) strip for different image plane distances from the sample**

The normalized intensity for the slit at different ' $z$ ' values are plotted in Fig. 2.2 (a). As we can see from plot the effect of diffraction is more profound in the near field i.e. when  $z = a$ . The effect of diffraction is very blur in the far filed region when  $z = 100*a$ .

### 2.3 Diffraction by Strip:

For the case of strip limits of integration are changed

$$\begin{aligned} & \sqrt{\frac{jk}{2\pi z}} \left( \int_a^\infty + \int_{-\infty}^{-a} \right) \exp\left(-\frac{jk(x-x_0)^2}{2z}\right) dx_0 \\ &= \frac{F(\infty) - F(v_+) + F(v_-) - F(-\infty)}{1-j} = 1 - D(x, z) \end{aligned} \quad (15)$$

Where we used  $F(\infty) = -F(-\infty) = (1-j)/2$

Thus, the diffracted field in case of strip

$$E(x, z) = \exp(-jk/z)[1 - D(x, z)] \quad (16)$$

$$\text{Intensity } (I) = E \times E^* \quad (17)$$

The normalized intensity for the strip is plotted in Fig 2.2 (b) for different values of ‘z’

## 2.4 Mathematical Model:

The total reflected intensity imaged by CCD is coming from two different surfaces with different reflectivity, the gold film and substrate. Accordingly, the mathematical model consists of two parts (Fig 2.3): the reflectance intensity coming from the metallic gold film and the reflectance intensity coming from the background substrate. The two intensities are combined to yield the total reflected intensity. Light coming from the gold film is treated as diffraction through a slit due to the high reflectivity of gold. In the latter case, the reflected light coming from the substrate is obstructed by gold thin film on its way to the microscope. Hence the reflection coming from the substrate is treated as diffraction past a strip.

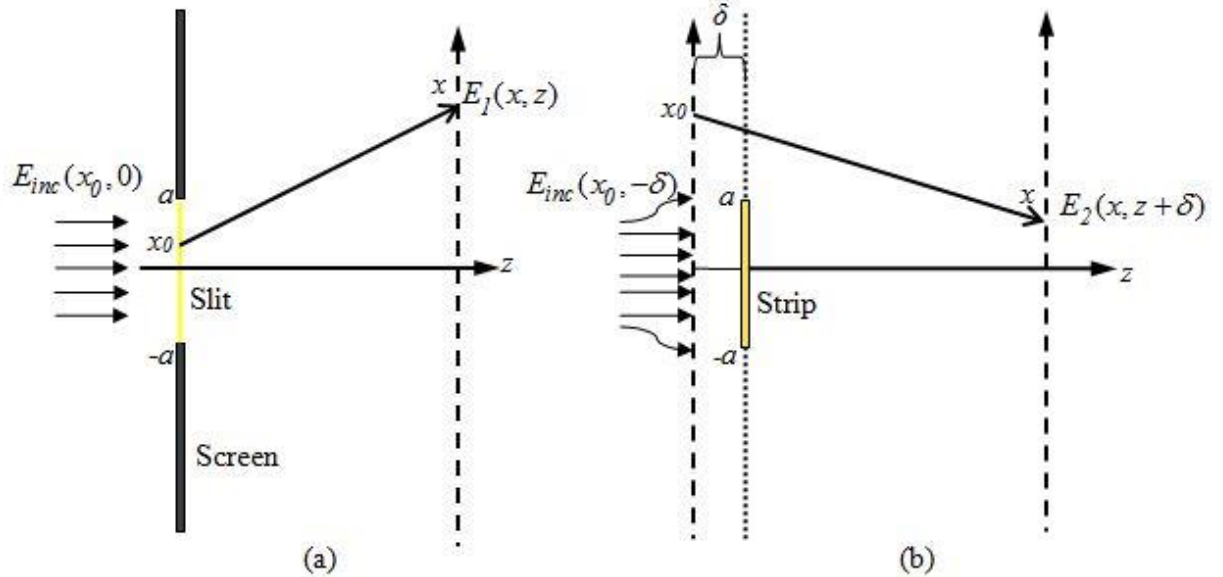


**Figure 2.3 Mathematical model set-up composed of reflection from the sample and substrate based on two simple diffraction model (a) The diffracted field for the gold line, where gold line is treated as slit (b) The diffracted field for the substrate, where gold line is treated as a strip blocking the light reflected from the substrate.**

For the first part Eq. 13-14 is used while for the second part Eq. 16-17 needs to be modified to take into account the difference in the distance traveled by the light before coming to CCD. The signal coming from the substrate is travelling a longer distance  $2 \cdot \delta$  as compared to the signal originating from the gold line which results in a phase shift between the two signals. The longer distance travelled accounts for the transparent silicon-dioxide layer between the gold film and the reflective silicon substrate.

In the case of the strip,

$$E_2(x, z + 2\delta) = \exp(-j(kz - \varphi)) \left[ \frac{F(\infty) - F(v_+) + F(v_-) - F(-\infty)}{1 - j} \right] \quad (18)$$

The total diffracted field can be obtained as

$$E_{total} = E_1 + \Gamma \cdot E_2 \quad (19)$$

where  $\Gamma$  is the ratio of the reflectivity of gold and the substrate material.

Then the total reflected intensity

$$I_{total} = E_{total} \cdot E_{total}^* \quad (20)$$

In the experiment the intensity measured by CCD is in arbitrary units. The model quantified total intensity in physical units. To compare the model with the experimental data, the total reflected intensity obtained from model is multiplied by the gain factor  $\gamma$

$$I_{model} = \gamma I_{total} \quad (21)$$

### 3. RESULTS & ANALYSIS

The two-dimensional Joule-heating data for the sample were taken using the experimental setup for the wavelengths of 470 and 530 nm. For a single wavelength, the results are repeatable for increasing and decreasing current; however, for the same sample the temperature distribution under two different LED wavelengths resulted in inconsistency.

In calculations the following two unknowns in the experiment are considered as fitting parameters: optical distance  $z$ , the distance between the observed specimen and the imaged plane, and phase shift  $\varphi$ , the shift in phase between the signal coming from the gold line and the substrate. The optical distance is dependent on the overall imaging of the microscope and is treated as a fitting parameter. The phase shift is dependent on the thickness of the oxide layer which is an increase in path length for the light to travel before reflecting off the silicon substrate. While treated as a fitting parameter, the phase shift must fall within a range consistent with this added path length. The effect of different  $z$  values is shown on each of the two components, in chapter-2 Fig. 2.2(a) for the slit  $a = 4\lambda$  and Fig. 2b for the same size strip. As can be seen from these figures the effect of diffraction is profound in the near field when  $z = a$ , whereas it is more blurred for the far field when  $z = 50a$ . The Fresnel number ( $F = a^2/\lambda z$ ) in our cases spans the range 0.1 to 3.5 which is on the order of 1. The Fraunhofer approximation is the limiting case when the optical distance  $z$  is large and  $F \ll 1$ . The Fresnel approximation is a partial series solution that is accurate in the limit  $F \gg 1$ , but can also be applied in the range  $F \sim 1$  with lower accuracy due to the truncated terms in the series [27, 29]. For a consistent approach we have used the Fresnel calculation. The optical distance  $z$  is an unknown in the experiment and is used as a fitting parameter when the model is compared to the data.

To fit the model parameters with experimental data least squares minimization is used to determine the best values for  $z$  and  $\varphi$ , starting from initial estimates of their values. This procedure is implemented in MATLAB. Since the experimental data are given in terms of averages of images from a CCD camera the least squares procedure also normalizes the absolute image strength with a gain parameter and accounts for the

difference in reflectivity of the gold and the silicon substrate which is consistent with published reflectivity for the two materials.

The other two fitting parameters, reflectance ratio  $\Gamma$  and gain parameter  $\gamma$ , are for normalizing the overall intensity in the model with experimental data. The total reflectance intensity comes from two different surfaces, gold line and substrate, with different reflectivities. Further, to consider the optical absorption and the intensity of light source, the two diffracted field intensities are combined in the model with the help of the reflectance ratio  $\Gamma$ . The values of the material's reflectivity at ambient temperature of 25 °C depend upon the wavelength and are available in literature [30]. The last fitting parameter is  $\gamma$  a gain parameter that converts the normalized intensity signal to the range on the CCD.

During the experiment the combined effects of vibration and noise smooth out the data, and result in an intensity profile that lacks small scale intensity signal variation seen in the model. This real filtering is due to the integration over the CCD pixels, physical vibration in the system, and diffraction in the optics. Therefore some additional spatial average is applied to the model data. The spatial average is performed by calculating moving average over a window of 11 pixels where each pixel is 0.0539  $\mu\text{m}$  in width. As the LEDs used in the experiment are not monochromatic the diffracted field and hence the reflectance intensity calculated with the mathematical model is integrated over the spectral width and strength of the LEDs. An attempt was made to take into account the incoherent nature of LEDs by performing phase average. Accounting for this wavelength variation did not significantly changes the nature of the intensity profile.

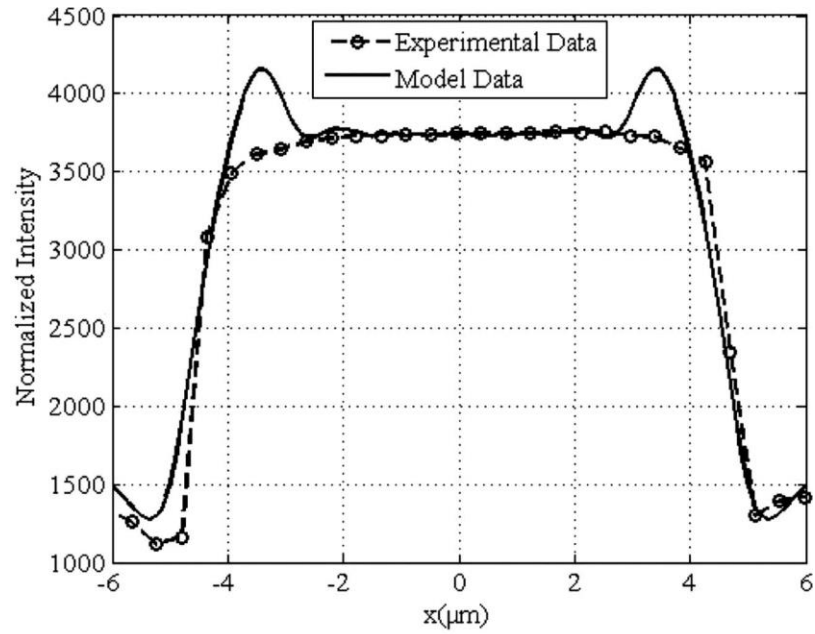
In Fig. 3.1. The model is compared with the experimental data at the wide section for wavelength of 535 nm. The parameters used to generate this figures are summarized in Table 3.1. Although not an exact match, the model shows very good qualitative agreement with the experimental data. At the edge of the gold line the model both underestimate and overestimates, the intensity. This is caused mainly by the edge diffraction effect and limited experimental data available for the substrate signal. This small scale oscillatory behavior is smoothed in the experimental data because of

averaging in the CCD, vibration in the system, variation in the coherence of the light, and diffraction due to thermal gradient in the air above the sample.

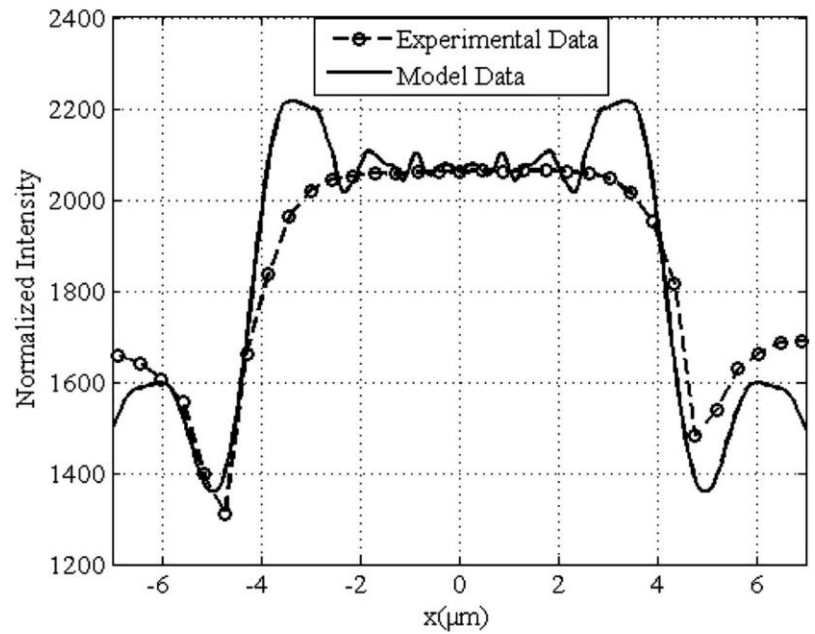
In Fig. 3.1b the model data are compared with the experimental data at the same wide section but for a different illumination wavelength, 470 nm. Similar matching of the model and the experiment is observed. As the wavelength of illumination changes the reflectance, optical distance and phase shift should change. The new values of these parameters for the fitting is obtained from the algorithm confirmed the theoretical values. The values are summarized in Table 1.

**Table 3.1: Summary of Fitting parameters**

Wavelength (nm)	$a$ ( $\mu\text{m}$ )	$z$ ( $\mu\text{m}$ )	$\phi$ (rad)	$r$	$\gamma$
535	5	20	2.2	0.64	3700
	0.5	3.75	2.2	0.64	3400
470	5	15	2.12	0.9	2068
	0.5	5.75	2.12	0.9	1068



(a)



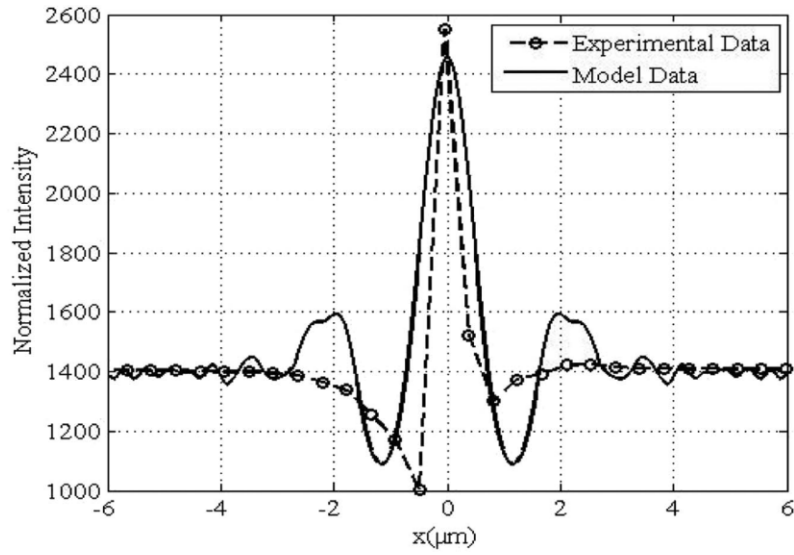
(b)

**Fig. 3.1** Plot of experimental data and model for 10  $\mu\text{m}$  wide gold interconnect for (a.)  $\lambda = 535\text{nm}$  at section a-a of Fig. 1.1 (c) and (b.)  $\lambda = 470\text{ nm}$  at section a-a of Fi. 1.1 (c)

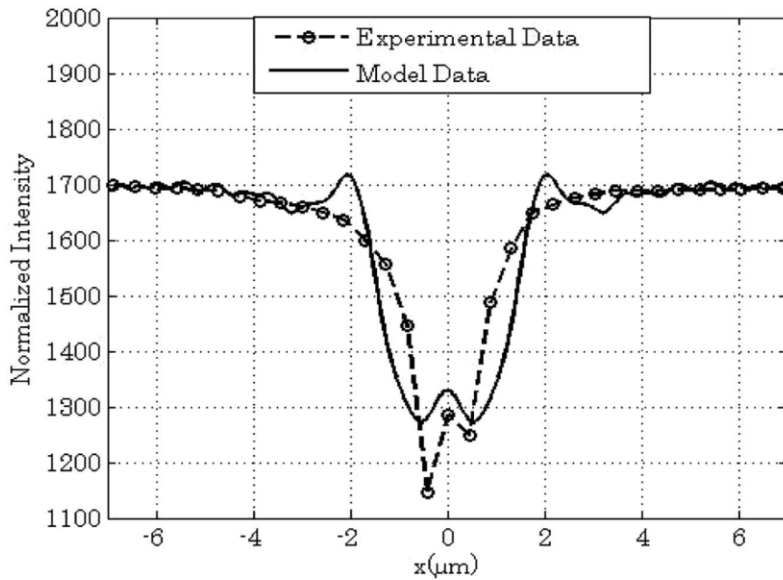
Fig. 3.2 (a) shows the fit for the narrow-field at wavelength of 530 nm. When moving from wide-section to narrow section for the same wavelength the optical distance should change and as result the phase shift. The values of these two parameters are varied

to fit the model data to the experimental data. As can be seen the model data fits with the experimental data except at the edge; again the model overestimates the experiment peaks.

Fig. 3.2 (b) shows the comparison of model and experimental data at narrow-section for the wavelength of 470 nm. The overall reflectivity of gold at 470 and 530nm is very different, around 0.4 to 0.6 and combined with the temperature dependence of the reflectivity, the diffraction patterns of both wavelengths along the gold line are different. By varying the optical distance  $z$  same amount as done for 530 nm the model doesn't provide a good fit with the experimental data. Different values of  $z$  were tested and the values listed in Table 2 give qualitative good fit for the data.



(a)



(b)

**Fig. 3.2 Plot of experimental data and model for 1  $\mu\text{m}$  wide gold interconnect for (a)  $\lambda$  \_ 535 nm at Section b-b of Fig. 1.1(c) and (b)  $\lambda$  \_ 470 nm at Section b-b of Fig. 1.1(c).**

The use of thermorefectance for temperature measurement has been well established based on its ability to generate a full field measurement, but there is an increasing desire to apply this technique to smaller spatial scales. As a result there is a need to understand the impact of optical limits on the signal generated. This is the first known work applying a diffraction model to understand the thermorefectance signal and it will be useful in extending the technique to smaller

scales. The diffraction model considers the reflection signal produced from samples of thin films on and from the substrate.

Four parameters are used in the model for fitting with experimental data. The results show good agreement between calculated and measured values. The overall reflectivity of gold at 470 and 530 nm changes significantly from 0.4 to 0.6 and this change is captured by the model. The diffraction patterns for 470 and 530 nm produce different data profiles. Furthermore, the thermoreflectance signal at each wavelength over the narrow line, one micron is significantly different than the wide-field due to the impact of the diffraction.

#### 4. Conclusions & Future work

The use of thermoreflectance for temperature measurement has been well established based on its ability to generate a full field measurement, but there is continuous demand to improve the spatial resolution to keep up the pace with the size of current optoelectronic and electronic devices. As the spatial resolution is limited by onset of optical diffraction, it is necessary to better understand the limit imposed by diffraction and propose solutions to overcome this barrier. This is the first work applying a diffraction model to understand the thermoreflectance signal. In most of electronic and optoelectronic applications thin metal film is protected by dielectric layer. The reflectance signals coming from the metal film is interfered by the diffused signal coming from the dielectric substrate. Due to this interference, the calibration procedure or in other words to find the thermoreflectance coefficient for the given metal is very complex experimental methodology. In current work model is developed considering the optical interference coming from dielectric - substrate layer along with the reflectance coming from the thin metal film.

Four parameters are used in the model for fitting with experimental data. The results show good agreement between results calculated using the developed model and experimental data. The overall reflectivity of gold at 470 nm and 530 nm changes significantly from 0.4 to 0.6, and this change in reflectivity is reproduced in model calculated values. During the experiment the temperature profile mapped with illumination wavelength of 470 and 530 nm are quite different. As well as, the diffraction pattern for each wavelength is significantly different for the narrow (1  $\mu\text{m}$  wide) line as compared to the wider (10  $\mu\text{m}$  wide) line. All these experimental observations are well captured by the model. This model will help to improve the spatial resolution of the thermoreflectance method and further will lead to simplify the calibration method in the given spectral range of illumination wavelength.

When this work is done thermoreflectance method is limited to the visible range of wavelength. The model is developed considering the two illumination wavelengths only. This work can be further extent to the other wavelength in the visible range and even to go for nanometers spatial resolution UV range. This model is developed for gold thin film on based of theory of diffraction by slit and strip. In future to understand the thermoreflectance signals coming from Carbon Nano Fibers (CNFs), nanorods and nanodots model can be extent with diffraction by circular aperture.

## REFERENCES

1. International Technology Roadmap for Semiconductors, 2013, available at <http://www.itrs.net/Links/2013ITRS/2013Chapters/2013Interconnect.pdf>
2. O. Nakabeppu, and T. Suzuki, "Microscale temperature measurement by scanning thermal microscopy", *J. Therm. Anal. Calorim.* **69**, 727-737 (2002).
3. D. Cahill, K. Goodson, and A. Majumdar, "Thermometry and thermal transport in micro/nanoscale solid-state devices and structures" *J. Heat Transfer*, **124** 223-241 (2002).
4. J. Christofferson, K. Maize, Y. Ezzahri, J. Shabani, X. Wang, and A. Shakouri, "Microscale and nanoscale thermal characterization techniques," in *Thermal Issues in Emerging Technologies*, Cairo, Egypt, 2007, pp. 3–9.
5. L. Wenjun, and B. Yang, "Thermography techniques for integrated circuits and semiconductor devices." *Sensor Review* 27, no. 4 (2007): 298-309.
6. M. Farzaneh, K. Maize, D. Lüerßen, J. A. Summers, P. M. Mayer, P. E. Raad, K. P. Pipe, A. Shakouri, R. J. Ram, and Janice A. Hudgings. "CCD-based thermorefectance microscopy: principles and applications." *Journal of Physics D: Applied Physics* 42, no. 14 (2009): 143001.
7. J. Christofferson, and A. Shakouri "Thermorefectance based thermal microscope" *Rev. Sci. Instrum.* **76** 1-6 (2005).
8. C. Cardenas, D. Fabris, S. Tokairin, F. Madriz, and C. Y. Yang, "Thermorefectance measurement of temperature and thermal resistance of thin film gold", *J. Heat Transfer*, **134**, No. 11, (November, 2012).
9. C. Cardenas, "Thermorefectance Temperature Measurement and Application to Gold Thin Films and Carbon Nanofibers" M.S. Thesis, Dept. of Mechanical Engineering, Santa Clara University, (2011).
10. G. Tessier, S. Holé, and D. Fournier, "Quantitative Thermal Imaging by Synchronous Thermorefectance with Optimized Illumination Wavelengths," *Applied Physics Letters*, 2001, doi:10.1063/1.1363696.

11. G. Tessier et al., "Measuring and Predicting the Thermoreflectance Sensitivity as a Function of Wavelength on Encapsulated Materials," in *Review of Scientific Instruments*, 2003, doi:10.1063/1.1517153.
12. G Tessier et al., "Thermoreflectance Temperature Imaging of Integrated Circuits: Calibration Technique and Quantitative Comparison with Integrated Sensors and Simulations," *J. Phys. D: Appl. Phys* **39** (2006): 4159–66, doi:10.1088/0022-3727/39/19/007.
13. T. Favalaro, , J-H. Bahk, and A. Shakouri. "Characterization of the temperature dependence of the thermoreflectance coefficient for conductive thin films." *Review of Scientific Instruments* 86, no. **2** (2015): 024903.
14. P. L. Komarov, M. G. Burzo, and P. E. Raad, "CCD thermoreflectance thermography system: Methodology and experimental validation" *THERMINIC 12*, Nice, France, 2006.
15. K. Maize, J. Christofferson, and A. Shakouri, "Transient thermal imaging using thermoreflectance." In *Semiconductor Thermal Measurement and Management Symposium*, 2008. *Semi-Therm 2008*. Twenty-fourth Annual IEEE, pp. 55-58. IEEE, 2008.
16. K. Yazawa, D. Kending, D. Hernandez, K. Maize, and A. Shakouri, "Challenges and opportunities for transient thermal imaging of microelectronic devices", *Thermal Investigations of ICs and Systems (THERMINIC)*, 2012 18th International Workshop on, **1, 4**, 25-27 (Sept. 2012).
17. A. J. Schmidt, R. Cheaito, and M. Chiesa, "Characterization of Thin Metal Films via Frequency-Domain Thermoreflectance," *Journal of Applied Physics*, 2010, doi:10.1063/1.3289907.
18. D. Kim et al., "Quantitative Thermal Characterization of Microelectronic Devices by Using CCD-Based Thermoreflectance Microscopy," doi:10.1117/12.2041052.
19. K. Maize et al., "Thermoreflectance CCD Imaging of Self-Heating in Power MOSFET Arrays," *IEEE TRANSACTIONS ON ELECTRON DEVICES* 61, no. **9** (2014), doi:10.1109/TED.2014.2332466.

20. S. Grauby, A. Salhi, L. P. Lopez, W. Claeys, B. Charlot, S. Dilhaire, "Comparison of thermorefectance and scanning thermal microscopy for microelectronic device temperature variation imaging: Calibration and resolution issues", *Microelectronics Reliability* **48**, 204-211 (2008).
21. Ziabari *et al.*, "Sub-diffraction limit thermal imaging for HEMT devices," *Thermal Measurement, Modeling & Management Symposium (SEMI-THERM), 2015 31st*, San Jose, CA, 2015, pp. 82-87.
22. J. W. Goodman, "Introduction to Fourier Optics", 3<sup>rd</sup> Edition, Roberts and Company, (2005).
23. F. R. Madriz, J. R. Jameson, S. Krishnan, X. Sun, and C. Y. Yang, "Circuit modeling of high-frequency electrical conduction in carbon nanofibers", *IEEE transactions on electron devices.*, **56**, **8**, ( August 2009).
24. F. R. Madriz, J. R. Jameson, S. Krishnan, X. Sun, and C. Y. Yang, "Test structure to extract circuit model of nanostructures operating at high-frequencies", in *IEEE Int. Conf. Microelectron. Test Struct.*, 138-40 (March 2009).
25. S. Tokairin, K. Read, P. Wilhite, J. Chen, D. Fabris, and C. Y. Yang, "Thermorefectance of carbon nanofibers: Joule Heating experiment and calibration", 10<sup>th</sup> International Conference on Heat Transfer, Fluid Mechanics and Thermodynamics, Orlando, Florida, (14 – 16 July 2014).
26. Beran, "The reflectance behavior of gold at temperatures up to 500 °C" *TMPM Tschermaks Mineralogische und Petrographische Mitteilungen*, **34**, 11-215 (1985).
27. F. L. Pedrotti, L. M. Pedrotti and L. S. Pedrotti, "Introduction to Optics", 3<sup>rd</sup> Edition, Addison-Wesley, (2006).
28. M. Born and E. Wolf, "Principles of Optics", 7th Edition, (1999).
29. S. J. Orfanidis, *Electromagnetic Waves and Antennas*, available online at [www.ece.rutgers.edu/~orfanidi/ewa](http://www.ece.rutgers.edu/~orfanidi/ewa) (2008).
30. E. Palik, "Handbook of Optical Constants of Solids", Elsevier, (1998).

## APPENDICES:

### A.1 Experimental Details:

The experimental setup to perform normal reflectance intensity analysis as a function of sample temperature is shown in Fig. A.1. It consists of an LED illumination source, CCD, optical microscope, sample holder and acquisition equipment. A modified Meiji Techno microscope Series MC-50T is used as the central component of the system. A beam splitter is placed at the core of the microscope to guide collimated incident rays and an aperture constrains the illumination beam onto the surface of the samples. Reflected light is transferred through the beam splitter to the CCD. A 12-bit A/D Prosilica GE1380 CCD camera is used to capture the reflectance intensity images. Illumination is generated from Luxeon® Star/O series LEDs. The spectral characteristics, as mentioned by manufacturer, of the two LEDs used in this research is enlisted in Table A.1. A custom designed heater microscopy stage assembly is used to support samples while providing thermal control over a temperature range from ambient 20 to 250 °C [8].

**Table A.1. Spectral characteristics of LEDs**

Color	$\lambda_{\min}$ (nm)	$\lambda_{\text{peak}}$ (nm)	$\lambda_{\max}$ (nm)	Spectral Half Width $\Delta \lambda_{1/2}$ (nm)
Blue	460	470	490	25
Green	520	530	550	35

The TR calibration coefficient  $\kappa$  is acquired prior to performing the measurements. Calibrations were performed for the two LEDs of central wavelengths 470 and 535 nm. Measurements of the sample temperature,  $T$ , and the normal reflectance intensity  $I_n(T)$  over sufficiently large regions of the material were used to compute  $\kappa$ . Under LED illumination with a peak wavelength of 535 nm, the average value of the calibration coefficient was  $-1.71 \times 10^{-4} \text{ } ^\circ\text{C}^{-1}$  with a standard deviation of  $0.19 \times 10^{-4} \text{ } ^\circ\text{C}^{-1}$ . Under LED illumination with 470 nm, the average value of the calibration

coefficient was  $1.76 \times 10^{-4} \text{ } ^\circ\text{C}^{-1}$  with a standard deviation of  $2.1 \times 10^{-5} \text{ } ^\circ\text{C}^{-1}$ . These values demonstrate good agreement with the previous results of Beran for gold [26].

The second mode of the experiment is to acquire two-dimensional TR images of the calibrated structure during Joule heating. During this mode of operation, a function generator, amplification circuitry and a delay generator are used to create a delay locked loop tuned to acquire images of the periodically heated sample during the quasi-steady heating and relaxation regimes. A reflectance intensity image of the sample acquired under illumination at  $\lambda_{\text{peak}} = 530 \text{ nm}$  is shown in Fig. 1c. Following the acquisition of the heated and relaxed state images, processing was done for the computation of the temperature difference using TR coefficient and Eq. 2 and 3. During Joule heating experiments adequate manual correction of positioning with superposition of a reference image and a focal metric calculation are performed to correct for displacements due to the thermal expansion. The thermal expansion of the system is estimated to be 0.3% and does not result in a significant change in system size relative to the wavelengths considered. Due to high optical absorption of gold in the visible range it was assumed during experiment that the surface reflection is dominant and the film is sufficiently thick to be considered optically opaque. At 100 nm the film thickness is 4.6 times the material's absorption coefficient which governs the exponential decay of the electromagnetic wave in the gold. TR response has been shown to be linear over the calibration temperature range of 20-200 °C.

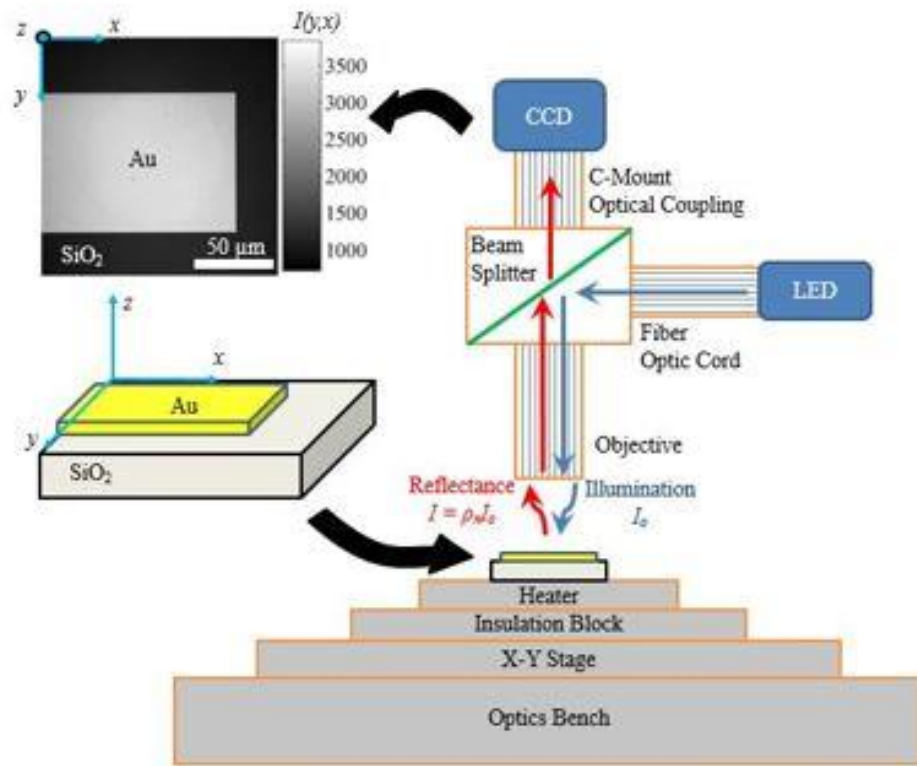


**Fig. A.1 Schematic of Thermoreflectance temperature measurement experimental set-up**

## A.2 MATLAB Code

### 1. To generate the figure:

```

I_530=figure_1(0.530,5,20,0.64,3700,(3*pi)/4);
I_470=figure_470(0.470,4.73,5,0.9,555,2.22);
load 530Rows
I_Exp_1=avgrW(:,1);
subplot(2,1,1);
plot(xs(1:8:end),I_Exp_1(1:8:end),'k--o',xs,I_530,'k-', 'LineWidth',2);
line1=get(gca,'Children');
set(gca,'FontSize',12,'FontName','Times New Roman')

hold on
%%plot(xs(1:10:end),I_Exp(1:10:end),'k-
o','LineWidth',2);set(gca,'FontSize',12,'FontName','Times New Roman')

set(findall(gcf,'type','text'),'FontSize',12,'FontName','Times New
Roman')
%%xlabel('x(μm)');
ylabel('Intensity(A.U.)');
xlim([-8,8]);
%%title('Comparison of Model data and Experimental data at wide section
for wavelength lambda=530');

```

```

title('\lambda=530nm');
%%grid on
load 470Rows
I_Exp_2=avgrW(:,1);
subplot(2,1,2);
plot(xs(1:8:end),I_Exp_2(1:8:end),'k--o',xs,I_470,'k-','LineWidth',2);
line2 = get(gca,'Children');
set(gca,'FontSize',12,'FontName','Times New Roman')
set(findall(gcf,'type','text'),'FontSize',12,'FontName','Times New
Roman')
xlabel('x(μm)'); ylabel('Intensity(A.U.)');
xlim([-7,7]);
title('\lambda=470nm');
h = [line1;line2];
%legend(h,'Model data','Experimental data','location','NorthOutside')
legend('Experimental Data','Model Data');
%%grid on

```

### Functions:

```

function [ I_new ] = figure_1(lambda,a,z,c,g,p)
k=(2*pi)/lambda; N_F=(a^2)/(lambda*z);
load 530Rows % **
w=sqrt(2*N_F);
v1=w*N_F.*(1-(xs/a)); % **
v2=w*N_F.*(1+(xs/a)); % **
F1=fcs(v1);
F2=fcs(v2);
D=(F1+F2)./(1-j);% **
E1=exp(j*k*z).*D;
I1=E1.*conj(E1);
E2=exp(j*(k*z-p)).*(1-D);
I2=E2.*conj(E2);
E=E1+c.*E2;
II=E.*conj(E);
I=g.*II;
I_new=moving_average(I,13);
end

```

```

function [ I_new ] = figure_470( l,a,z,c,g,p )
k=(2*pi)/l;
load 470Rows;
w=sqrt(k/pi/z);
v1=w.*(a-xs); % **
v2=w.*(-a-xs); % **
F1=fcs(v1);
F2=fcs(v2);
D=(F1-F2)./(1-li)+(F1+(1-li)/2-F2);% **
E1=exp(-li*k*z).*D;
I1=E1.*conj(E1);
E2=c.*exp(-li*(k*z-p)).*(1-D);
I2=E2.*conj(E2);
E=E1+ E2;
II=E.*conj(E);

```

```

I=(g.* II);
I_new=moving_average(I,13);

end

```

### Fraunhofer diffraction code:

```

function F = fcs(x)

if nargin==0, help fcs; return; end

F = zeros(size(x));           % defines the size of F

F = fcs2(pi*x.^2/2);

i = find(x<0);
F(i) = -F(i);                 % F(x) is an odd function

function F = fcs2(x)

if nargin==0, help fcs2; return; end

a = [ 1.595769140, -0.000001702, -6.808568854, -0.000576361,
      6.920691902, -0.016898657, ...
      -3.050485660, -0.075752419,  0.850663781, -0.025639041, -
      0.150230960,  0.034404779];

b = [-0.000000033,  4.255387524, -0.000092810, -7.780020400, -
      0.009520895,  5.075161298, ...
      -0.138341947, -1.363729124, -0.403349276,  0.702222016, -
      0.216195929,  0.019547031];

c = [ 0,
      -0.024933975,  0.000003936,  0.005770956,
      0.000689892, -0.009497136, ...
      0.011948809, -0.006748873,  0.000246420,  0.002102967, -
      0.001217930,  0.000233939];

d = [ 0.199471140,  0.000000023, -0.009351341,  0.000023006,
      0.004851466,  0.001903218, ...
      -0.017122914,  0.029064067, -0.027928955,  0.016497308, -
      0.005598515,  0.000838386];

A = fliplr(a+j*b);
C = fliplr(c+j*d);

x = abs(x);

F = zeros(size(x));

m = find(x<=4);

```

```
n = find(x>4);  
  
F(m) = exp(-j*x(m)) .* sqrt(x(m)/4) .* polyval(A, x(m)/4);  
F(n) = exp(-j*x(n)) .* sqrt(4./x(n)) .* polyval(C, 4./x(n)) + (1-j)/2;
```

# **DIFFRACTION MODEL FOR THERMOREFLECTANCE DATA**

By

**Sahida Rahimbhai Kureshi**

Submitted

To

Department of Mechanical Engineering

Santa Clara University

In the requirement of the partial fulfillment of the

**Engineer's Degree in Mechanical Engineering**

## **ABSTRACT**

Diffraction based mathematical model is developed to address the issue of spatial resolution in thermoreflectance imaging at the scale of 1 and 10  $\mu\text{m}$ . Thermoreflectance imaging provided non-contact temperature measurement at micro and nano scale but the spatial resolution is limited by diffraction. By virtue of this work mathematical model is developed for the analysis of thermoreflectance data. In the development of model both the diffraction occurring at sample and substrate is combined to calculate intensity of thermoreflectance signal. This model takes into account the effective optical distance, sample width, wavelength, signal phase shift and reflectance intensity. Model shows qualitative and quantitative agreement with experimental data for the two wavelengths under investigation, 470 nm and 535 nm.

# DEDICATION

This dissertation is dedicated to my husband, Rizvan, and our children, Rushan and Rifa. I express my deepest expression of love and appreciation for the encouragement you gave me during this study. You were the strong pillar of my motivation to complete this study. Thanks for your patience and support.

## **ACKNOWLEDGEMENTS**

My deepest gratitude is to my advisor, Dr. Drazen Fabris. I have been amazingly fortunate to have Dr. Fabris as my supervisor. His continuous support and encouragement during my study at Santa Clara University helped me to overcome many crisis situation. I wouldn't imagine this degree to be complete without his motivation and the trust he put on me. I am grateful to him for holding me to a high research standard and enforcing strict validations for each research result, and thus teaching me how to do research. Under his supervision I publish my first peer reviewed article.

I am grateful to Dr. Cary Yang for allowing me to work in his group. I am also thankful to him for encouraging the use of correct grammar and consistent notation in my writings and for carefully reading and commenting on countless revisions of the journal article manuscript.

I would like to acknowledge my fellow researchers Chris Cardenas and Shawn Tokairin to provide experimental data for validation of my model and giving comment on article manuscript.

Most importantly, none of this would have been possible without the love and patience of my family. My immediate family to whom this dissertation is dedicated to, has been a constant source of love, concern, support and strength all these years. I would like to express my heart-felt gratitude to my family. I must give special thanks to my parents at back home in India who has aided and encouraged me throughout my life and in this endeavor.

Finally, I appreciate the financial support from Dean of Engineering and Packard fellowship.

## TABLE OF CONTENT

1. Introduction	1
1.1 Introduction	1
1.2 Thermoreflectance Method	6
1.3 Diffraction	12
2. Mathematical Model	
2.1 Diffraction Theory	15
2.2 Diffraction by slit	18
2.3 Diffraction by strip	20
2.4 Mathematical Model	20
3. Results and Analysis	23
4. Conclusion and Future work	30
References	31
Appendices	
A.1 Thermoreflectance Experimental set-up	34
A.2 MATLAB code	36

## LIST OF TABLES

Table 1.1	Summary of popular high-resolution thermal measurement techniques in micrometer-nanometer range	1
Table 3.1	Summary of Fitting parameters	25
Table A.1	Spectral characteristics of LEDs	33

## LIST OF FIGURES

Fig. 1.1	Gold line sample used for electrical interconnect testing and thermoreflectance testing in prior work [7,14] (a) Top view of sample (b) section-view of sample (c) microscopy obtained reflectance intensity image under LED wavelength of 535 nm. Section a-a captures a region of the gold line structure at 10 micron wide whereas in section b-b the width is 1 micron	13
Fig. 2.1	Diffraction field for Rayleigh-Sommerfeld diffraction Integral	16
Fig. 2.2	Effect of distance $z$ on diffracted field intensity (a) slit (b) strip for different image plane distances from the sample	19
Fig. 2.3	Mathematical model set-up composed of reflection from the sample and substrate based on two simple diffraction model (a) The diffracted field for the gold line, where gold line is treated as slit (b) The diffracted field for the substrate, where gold line is treated as a strip blocking the light reflected from the substrate.	21
Fig. 3.1	Plot of experimental data and model for 10 $\mu\text{m}$ wide gold interconnect for (a.) $\lambda = 535\text{nm}$ at section a-a of Fig. 1.1 (c) and (b.) $\lambda = 470\text{ nm}$ at section a-a of Fi. 1.1 (c)	26
Fig. 3.2	Plot of experimental data and model for 1 $\mu\text{m}$ wide gold interconnect for (a) $\lambda = 535\text{ nm}$ at Section b-b of Fig. 1.1(c) and (b) $\lambda = 470\text{ nm}$ at Section b-b of Fig. 1.1(c)	28
Fig. A.1	Schematic of Thermoreflectance temperature measurement experimental set-up	35



# 1. INTRODUCTION

## 1.1 Introduction:

Miniaturization has become synonyms of semiconductor devices in the current era. The size of electronic devices and line in current ICs has shrunk to 24nm [1]. The reduced size of devices out perform in terms of switching speed and fabrication cost. However, the shrunk size of electronic devices gives new challenges to heat management design. The main barrier in the development of micro and nano scale devices is the resulting large current density and local heating. In the last twenty years it has become more challenging for designers to understand the heat transfer and thermal characterization at micro and nano scale due to small size of electronic devices. Temperature mapping at micro and nano scale is very important for safe and reliable operation of small scale electronic devices [2, 3]. With electronic devices in the range of size few nano meters to micrometers the conventional methods of temperature measurement like Infrared radiation thermometry and the micro-Raman methods is no more useful.

Various methods of temperature measurement on the scale of current electronic and optoelectronic devices are surveyed by Christofferson et al. [4] and Wenjun et al. [5].

Table 1.1 present the summary of these methods:

**Table 1.1: Summary of popular high-resolution thermal measurement techniques in micrometer-nanometer range**

Method	Principle	Resolution			Imaging ?
		Spatial ( $\mu\text{m}$ )	Temperature (K)	Response time (s)	
Micro-thermocouple	Seebeck effect	50	0.01 0.02 (if blackbody )	5 m 10 $\mu\text{m}$ (single point)	No

Infrared thermography	Planck blackbody emission	3-10	-1 K	-0.5 m (image)	Yes
Liquid crystal thermography	Crystal phase transitions (change color)	2-5	0.5 (near phase transition)	3 m	Yes
Thermo-reflectance	Temperature dependence of reflection	0.3-0.5	0.01	0.006-0.1 $\mu\text{m}$	Yes
Scanning Thermal microscopy (SThM)	Atomic force microscope with thermocouple or Pt thermistor tip	0.05 (surface morphology)	0.1	10-100 $\mu\text{m}$	Scan
Fluorescence thermography	Temperature dependence of quantum efficiency	0.3	0.01	200 $\mu\text{m}$	Scan
Optical interferometry	Thermal expansion, Michelson type	0.5	0.0001 (1 fm)	0.006-0.1 $\mu\text{m}$	Scan
Micro-Raman	Shift in Raman frequency or ratio of Stokes/anti-Stokes amplitudes	0.5	1	1 $\mu\text{m}$	Scan
Near field probe (NSOM)	Use near field to improve optical resolution	0.05	0.1-1 (S/N dependent)	0.1-10 $\mu\text{m}$	Scan
Built-in temperature sensors	Fabricate a thermal sensor integrated into the device	100s	0.0002-0.01	1 $\mu\text{m}$	No

All the methods summarized in Table 1.1 can be broadly classified into two categories: (1.) contact measurement and (2.) non-contact measurement. Following are some advantages offered by Non-contact methods over contact methods:

- (i) Fast – allowing more measurements to take and therefore it is more convenient for large data acquisition (Temperature mapping)
- (ii) Measurements can be taken of object surrounded by hazardous material
- (iii) Non-destructive measurement

However, all the non-contact measurement methods are limited by onset of diffraction.

The most promising techniques regarding spatial resolution are those involving contact probes [6], which are usually limited to the measurement of surface temperatures. In integrated circuits, mainly the heat is generated due to joule heating in metal thin films and contacts, those are often buried under a few hundreds of nanometers or several micrometers of encapsulation dielectric. Therefore, the use of thermocouples and in-built sensors, integrated within the circuit is good option. After calibration, they deliver high precision and high sensitivity temperature measurements but provide no spatial information [6]. Moreover, due to the presence of interfaces, strong temperature gradients can exist in integrated circuits, leading to discrepancies between the temperature of the active region and that measured by the sensor.

Infrared (IR) thermometry is one of the most widely used technique for temperature measurements of electronic devices, particularly ICs [4]. IR thermometry is based on determining the spatial distribution of IR thermal radiation emitted from the surface of a solid [4]. Based on Planck's law of blackbody radiation, the maximum spectral power density of an ideal blackbody at thermal equilibrium will shift to lower wavelengths with increasing temperature. Since, in practice the surface of a device under study is not a blackbody and reflects some of the incident radiation, the blackbody law must be scaled by a material dependent factor known as the emissivity. Emissivity depends on the surface property and geometry, wavelength and temperature of the object, and must be known for each surface to obtain an accurate thermal profile. Silicon is largely transparent to near IR radiation, making IR thermography a valuable tool for thermal mapping of IC backplanes and hot spots. The thermal resolution of IR cameras can be 10-20 mK [4], but their spatial resolution is mainly determined by the diffraction limit for the range of wavelengths to which the detector is sensitive. The most sensitive IR cameras work at 3  $\mu\text{m}$  wavelength [4], which is not suited to the length scales of many

modern electronic and optoelectronic devices. Apart from the sub-optimal spatial resolution of IR thermography, other drawbacks include inaccuracy due to the attenuation of radiation between the target and the detector, uncertainty in the emissivity of the device surface and background radiation [5]. Furthermore, material likes most metals with high reflectivity and the low emissivity limits the application of IR thermography. Liquid crystal thermography (LCT) and fluorescence microthermography (FMT) are semi-invasive thin coating methods. In the LCT technique [4, 5], the surface of the device under study is covered with a thin layer of liquid crystal and illuminated with white light. At different temperatures, the liquid crystal layer reflects different wavelengths of this incident light. The theoretical limit for the resolution of the method was estimated to be 25  $\mu\text{m}$  spatially and 0.1 K in temperature [5]. To improve the spatial resolution of the method, the nematic–isotropic phase transition of liquid crystal which occurs at the clearing point of the crystal is used [5]. It is stated by Wenjun & Yang [5], and the reference there in, “Below clearing point the liquid crystal is in the nematic phase which scatters light and rotates the plane of polarization of the light and appears bright under a polarizing microscope. Above clearing point, where the liquid crystal is in the isotropic phase, the plane of polarized light does not change and the image field appears dark. Taking advantage of the nematic–isotropic phase transition has given the LCT method a spatial resolution of 2–4  $\mu\text{m}$ ”. Due to semi-invasive nature of LCT technique the thermal conductivity and heat capacity of the liquid crystal coating can affect the device under test. In addition, the uniformity and thickness of the liquid crystal layer are important factors in the accuracy and resolution of the technique [4]. Fluorescent microthermography (FMT) [4, 5] utilizes the temperature-dependent quantum efficiency of photoluminescent rare earth dyes. As mentioned by J. Christofferson *et al* [4], in FCT technique, “the sample surface is coated with a thin film of such dyes and is then illuminated by ultraviolet (UV) light”. FMT can be used for thermal imaging of electronic and bio sensing devices as well as hot spot detection and thermal mapping of ICs. A spatial resolution of 0.3  $\mu\text{m}$  and a thermal resolution of 1 mK have been reported for FMT [4], although sample preparation and optical system design require special

consideration. Photon shot noise, UV bleaching, film dilution and film preparation can have a significant impact on the quality of FMT thermal images.

Using micro-thermocouples as inexpensive point measurement contact probes can provide accurate temperature readings with a thermal resolution of 0.01 K [5]. However, as stated by Wenjun & Yang [5], the large size of the thermocouple wires ( $\sim 25\text{-}50\ \mu\text{m}$  diameter) results in a poor spatial resolution. In addition, due to difficulties in maintaining good thermal contact between the micro thermocouple junction and the surface of a device results in faulty readings. Finally, as point-based measurement tools, micro-thermocouples cannot be used for imaging without implementing complicated translation stages [5]. Scanning Thermal Microscopy (S<sub>Th</sub>M) is a contact thermometry technique with very high spatial resolution. S<sub>Th</sub>M utilizes the mechanism behind atomic force microscopy (AFM) and scanning tunneling microscopy (STM). The S<sub>Th</sub>M probe consists of a thermocouple fabricated on the tip of an AFM cantilever [6]. When the probe is scanned in contact mode over the surface of a sample, localized heat transfer between the sample surface and the probe tip leads to a change in the tip temperature that is measured by the thermocouple. In this way, both the tip-sample heat transfer across the entire surface and the sample topography can be obtained simultaneously with sub-micrometre spatial resolution ( $\sim 0.05\ \mu\text{m}$ ) and a thermal resolution of 0.1K [4]. However, the roughness of the sample surface can cause variations in the tip-surface thermal contact, leading to noise in the thermal signal. Furthermore, the S<sub>Th</sub>M experimental setup is complicated and expensive, and data acquisition can be time-consuming due to the required scanning methods [5]. A major limitation of S<sub>Th</sub>M is the liquid meniscus that forms between the tip and the sample, which is intrinsic to contact measurements done in atmosphere and limits the resolution of the technique. Finally, S<sub>Th</sub>M cannot be used easily on light emitting surfaces of optoelectronic devices such as vertical cavity surface emitting lasers (VCSELs), because the light is absorbed by the S<sub>Th</sub>M thermocouple and causes errors in temperature measurement [6]. Raman spectroscopy is an optical measurement technique that is well suited for temperature measurements in microelectronic devices, especially made from silicon, due to its strong scattering cross-section [5]. The Raman technique provides spatial resolutions on the order of 1  $\mu\text{m}$  or

smaller considering far field diffraction limited optics [5]. In addition to the above-mentioned techniques, other methods of thermography include acoustic thermography, near-field scanning optical microscopy (NSOM) adapted for temperature measurement, laser interferometry and thermoreflectance microscopy. This last thermography method is the focus of this research work and will be discussed in detail in the next sections.

### **1.1 Thermoreflectance Method:**

Thermoreflectance (TR) temperature measurement belongs to the class of non-contact temperature measurements and uses an LED or filtered white light source and a CCD to acquire images. TR techniques offers direct access to the active areas under the transparent encapsulation layers. In the visible or near UV range, excellent spatial resolutions can be reached. It has been shown that the thermal and spatial resolutions of CCD-based thermoreflectance can be as low as 10 mK and 250 nm, respectively [6], but the fundamental temperature limit has not been found yet. The major advantage of TR microscopy is: relatively short data acquisition times compared with other techniques and its suitability to a wide range of materials including metals and light emitting surfaces. Thermoreflectance temperature measurement is based on the principle that a change in temperature of a given material produces a small change in the spectral reflectivity of the material's surface [6-9]. This small change can be linearized over a range of temperature. The linearized response of the normal reflectance with respect to the temperature of a sample allows the following approximation for the derivative of normal reflectance [8]

$$\frac{\partial \rho_n}{\partial T} \approx \frac{\rho_n(T) - \rho_n(T_0)}{T - T_0} \quad (1)$$

The normal reflectance intensity at a given temperature,  $I_n ( T )$ , can be calculated from the normal reflectance,  $\rho_n(T)$  and incoming illumination intensity  $I_0$

$$I_n (T) = \rho_n (T) \cdot I_0 \quad (2)$$

The spectral thermoreflectance (TR) coefficient  $\kappa$  is defined by the normalization of the slope as a function of temperature with the reference quantity [8]

$$\kappa = \frac{1}{\rho_n(T_0)} \frac{\partial \rho_n}{\partial T} = \frac{1}{I_n(T_0)} \frac{\partial I_n}{\partial T} \quad (3)$$

During the experiment, it is necessary to calibrate the system and obtain the thermoreflectance coefficient for the specific sample. Following the calibration, one can determine the temperature difference developed during heating through rearrangement of the governing relationship with a measurement of the relative reflectance.

$$\Delta T = (T - T_0) = \frac{1}{\kappa} \left( \frac{I_n(T) - I_n(T_0)}{I_n(T_0)} \right) \quad (4)$$

The thermoreflectance coefficient is a material and surface property that depends on the illumination wavelength, temperature, microscope, material surface characteristics and in some cases also on the material processing [9]. For most metals and semiconductor materials of interest the value of the thermo-reflectance coefficient ( $\kappa$ ) will be in the order of  $10^{-2}$  to  $10^{-5} \text{ K}^{-1}$  [6-10].  $\kappa(\lambda)$  can vary sharply within the spectral region of interest particularly in the visible spectrum, and therefore the choice of illumination wavelength determines not only the spatial resolution of the technique but also the sensitivity of method. It is essential to choose a wavelength for which the change in reflectivity is highest for given change in temperature and reflectivity has minimum value [10]. In addition, electronic and optoelectronic device analyzed with TR microscopy generally have layered structures that strongly modifies the TR coefficient. The protection layer of integrated circuits is made of dielectric material which is transparent to visible light. The optical interference which occurs in these layers strongly modifies the reflectivity and can

even forbid thermorefectance measurements at some wavelengths. For each series of circuits, it is therefore necessary to determine the illumination wavelengths for which thermorefectance will deliver optimal signals [10, 11]. As stated in [10], one way to calibrate thermorefectance for range of spectrum is to use different LEDs as illumination sources, and measure the photothermal response at each LED wavelength. This has been demonstrated on a 45 nm thick NiCr oxide resistor deposited on a GaAs substrate with 1.5 $\mu$ m thick Au Ohmic contacts and blanked coated with a Si<sub>3</sub>N<sub>4</sub> passivation layer [10]. It is observed by G. Tessier *et al* [10], that red LEDs ( $\lambda = 615$  and 660 nm) exhibited low response for both bare and passivated Au, while an orange LED ( $\lambda = 598$  nm), was shown to be suitable for thermal imaging of passivated NiCr and Au. Further they found “green illumination ( $\lambda = 511$  nm) gave a large signal for Si<sub>3</sub>N<sub>4</sub>-coated GaAs and a small signal for passivated Au”. Therefore, it is possible to measure the thermal behavior of a selected material within a complex structure by careful choice of the illumination wavelength. This method is very time consuming and therefore subject to drifts. To improve the calibration method G. Tessier *et al.* [11] has developed a CCD camera-based thermorefectance microscope coupled to a grating which disperses white light directly onto the CCD. This instrument gives the complete spectra of the reflection coefficient and its temperature dependence, reflectivity and the ratio of change in reflectivity with respect to change in temperature can be measured on one or several materials with only one acquisition. The optimal wavelength for thermorefectance measurements can therefore be measured within minutes on any sample. A model considering multiple reflections and the thermal expansion of the encapsulation layer has been also developed in this work [11] to explain the spectra and variation of TR coefficient for given spectra on encapsulated circuits. This model can be used to predict qualitatively the optimal working wavelength. Alternatively, Peltier element control of the whole package temperature in order to obtain calibration coefficients simultaneously on several materials visible on the surface of the circuit is proposed [12]. Under high magnifications, movements associated with thermal expansion are corrected using a piezo electric displacement and a software image shift. In this work [12] the temperature obtained by thermorefectance have been compared with those obtained by two sensors, a thermistor

and a diode junction. The agreement with thermorefectance and simulation is very good, with a standard deviation of the order of 2.3%. As it is mentioned in [4-6], while thermorefectance is a very sensitive and high resolution tool for temperature mapping, its precision is still two orders of magnitude lower than its thermal resolution, mainly due to the complexity of calibration procedures. Efforts remain to be made to make precision and temperature resolution comparable. Noninvasive method for thermorefectance coefficient calibration ideally suited for in-chamber, and thus high temperature has been developed in [13]. Thermorefectance coefficients for three commonly encountered metals in electronic devices: gold, platinum, and aluminum is explained in this work [13]. The effect of passivation on these metals is also examined, and it is demonstrated the signal to noise ratio of a thermorefectance measurement can be improved with informed selection of the dielectric layer thickness. For gold, the behavior of TR coefficient is analyzed under 455, 470, and 530 nm illumination in the measurement chamber from room temperature to 500 K. For the given  $\Delta T$  inside the thermostat, bare gold illuminated at 530 nm has the highest thermorefectance response, followed by 470 nm and then 455 nm. Further, the reflectivity signal is significantly enhanced in the passivated region at 530 nm, but is slightly diminished at 470 nm with almost no change at 455 nm [13], relative to bare gold metal. The average rate of change in the TR coefficient of bare gold metal is measured of  $0.30 \times 10^{-4}$  per 100K temperature [13].

Frequency-Domain measurement techniques, lock-in method of thermorefectance microscopy has proven effective in obtaining thermal images of active electronic and optoelectronic devices with submicron spatial resolution and 10-50mK temperature resolution [6]. Thermorefectance systems that use a lock-in method capture the steady state thermal signal but provide limited information about the thermal transient.

However, it is often desirable to observe how devices thermally evolve in time. Due to the size of typical electronic and optoelectronic devices, thermal effects can occur on a millisecond or microsecond time scale or faster [6]. Thermorefectance methods based on time domain analysis can characterize fast transient heating effects such as the thermal rise time by reconstructing the time varying reflectance signal. Burzo *et al* [14] has demonstrated first experimental system capable of noninvasively and nondestructively

scanning the transient surface temperature of pulsed microelectronic devices with submicron spatial and sub-microsecond temporal resolutions. Burzo *et al* [14] have used the experimental set-up to scan the active area of typical MOSFET devices of differing gate widths and lengths. Both quasi steady-state and transient temperature measurement results are obtained with overall random uncertainty of the results to be less than 13% [14]. In order to partially overcome the slow frame rates associated with CCDs, Maize *et al* [15] have used a pulsed LED and a CCD camera to acquire transient thermal images almost 100 times faster than single point TTR, without the need for a laser and scanning translation stage. Their technique utilizes a pulsed boxcar averaging scheme in which the boxcar average is combined with a short duration LED pulse ( $\sim 10$  ns) synchronized with device excitation. For each exposure of the CCD, there is one LED pulse, effectively reducing the camera exposure to the time duration of the LED pulse width. For the next integration period of the CCD, the phase between the LED pulse and the device excitation is advanced by a small, known amount, and the in-between data points are filled in by combining multiple boxcar averages. By stepping the light pulse in regular increments, the CCD thus records the full thermal transient of the device with time resolution limited by the pulse width. This method has been used to demonstrate transient thermal imaging of a micro-heater with millisecond and microsecond time resolution, comparing rapid heat diffusion in the device metal to slower diffusion into the substrate [15]. An example of transient thermal imaging on a test chip is studied in [16]. This work [16] discusses the relationship of spatial resolution and time resolution considering the ‘time constant’ component of chip. Spatial resolution for thermoreflectance is limited by the diffraction of the illuminating light, time resolution is limited by the high speed electrical signal management, and temperature resolution is limited by the signal-to-noise ratio [16]. In the current work issue of spatial resolution is addressed and detail explanation is given in next sections.

Application of frequency-domain thermoreflectance is extended to the characterization of thin metals films on low thermal diffusivity substrates [17]. It is seen, how a single noncontact measurement can yield both the thickness and thermal conductivity of a thin metal film with high accuracy. Results are presented from

measurements of gold and aluminum films 20–100 nm thick on fused silica substrate. The thickness measurements are verified independently with atomic force microscope cross sections, and the thermal conductivity measurements are verified through electrical conductivity measurements via the Wiedemann–Franz law. The thermoreflectance thermal conductivity values were in good agreement with the Wiedemann–Franz results for all the films at least 30 nm thick, indicating that presented method can be used to estimate electrical conductivity along with thermal conductivity for sufficiently thick films.

Thermoreflectance measurement system can provide exact thermal information to identify defects in a device that are hardly perceptible with the IR thermography system and the conventional widefield microscope system [18]. By determining the thermoreflectance calibration coefficient experimentally, quantitative temperature distribution of polysilicon micro-resistors was obtained in [18]. Using their proposed thermoreflectance measurement system on a polysilicon micro-resistor, a high thermal resolution of up to ~13 mK was achieved in 50,000 iterations by using a high bit-depth CCD camera, and a high spatial resolution of ~670 nm was realized with a 100× (0.5 NA) objective lens and visible light source (635.9 nm). The obtained thermoreflectance calibration coefficient of polysilicon was  $-1.71 \times 10^{-3}$  with illumination light at  $\lambda=635.9$  nm and a 20× (0.42 NA) objective lens [18].

The application of thermoreflectance CCD imaging in power microelectronics is demonstrated in [19]. Thermoreflectance imaging with submicrometer spatial resolution and 50 mK temperature was used to study self-heating temperature distribution in LDMOS silicon power transistor arrays under dc operation. Thermoreflectance images revealed highly nonuniform spatial self-heating distribution in the active power arrays.

The major drawback of Thermoreflectance measurement technique are: sensitivity of method to illumination wavelength and the diffraction limited spatial resolution. The problem of diffraction is discussed by Grauby et al., but no suggestions was given to handle this issue [20]. Recently A. Ziabari et. al. [21], came up with idea of numerical simulation and analytical model to address the issue of diffraction in thermoreflectance imaging. They have developed analytical model based on Bessel's function and found thermoreflectance coefficient for sample and

substrate. Further did simulation using ANSYS APDL and then combine results with analytical model to obtain final temperature profile.

## **1.2 Diffraction:**

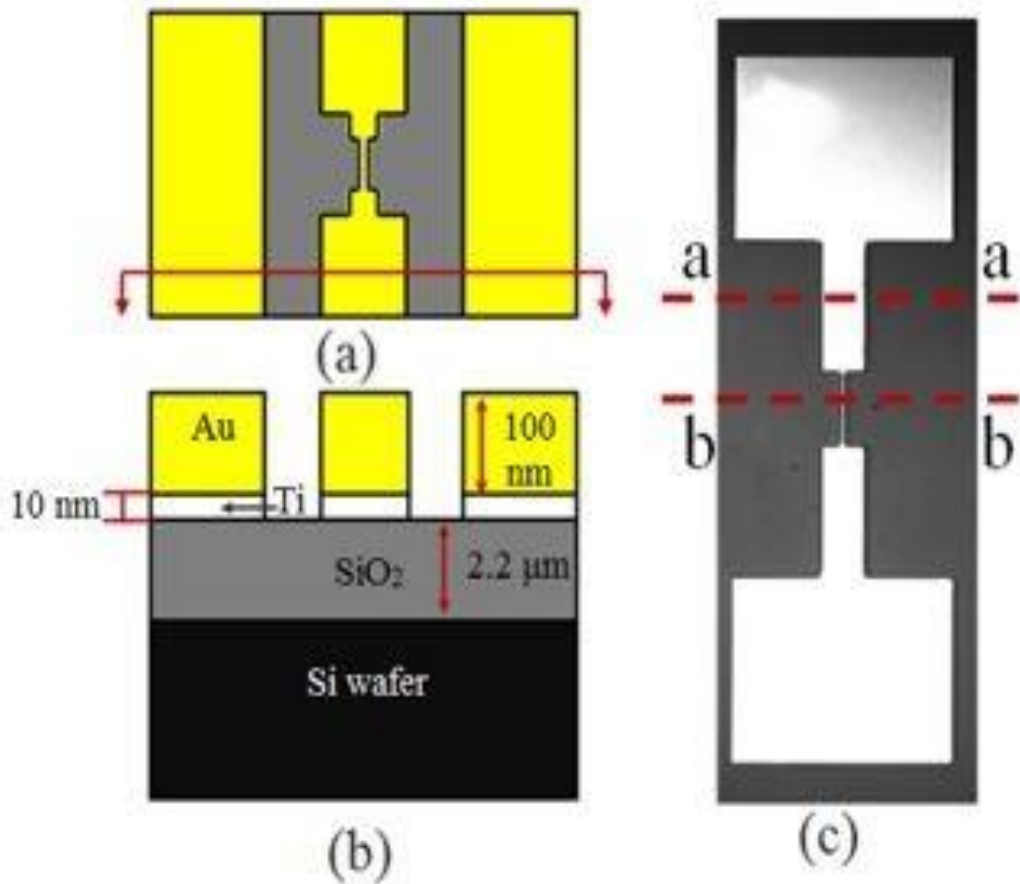
Diffraction effects are consequence of the wave nature of light. Diffraction means any deviation of light rays from rectilinear that cannot be interpreted as reflection or refraction [22], was long back first reported by Grimaldi in 1665. When some obstruction is present in the path of light wave, resulting pattern on the other side of obstacle can be explained with diffraction theory. The obstacle need not to be opaque but if causes local variations in the amplitude or phase of the wavefront of light such effects are observed. Because the diffraction cause the blurring at edges of any optical images, diffraction phenomenon leads to fundamental limitation in instrument resolution. Rayleigh criterion along with lens maker equation estimates the limit of resolution and it is approximately half of wavelength of light reflected from surface. Due to this resolution limitation set by diffraction abundant work is done to understand theory of diffraction and thereby to improve the resolution.

As mentioned in section 1.2 non-contact thermal measurements has spatial resolution limitation due to diffraction. Infrared Thermography has spatial resolution in the range of 3-10  $\mu\text{m}$  due to use of infrared range light source in imaging. Thermoreflectance Imaging temperature measurement also has spatial resolution limit due to diffraction. In the prior work, thermoreflectance was used to measure the temperature of thin gold films that modeled electrical interconnects. The modeled interconnects were 1 to 10  $\mu\text{m}$  in width and tens of  $\mu\text{m}$  long. In this work a mathematical model is developed for better analysis of the thermo-reflectance experimental data. The main purpose of this work is to understand the impact of diffraction and the parameters that govern the signal.

The model developed in the course of this thesis is based on Rayleigh-Sommerfeld diffraction formula that is the reformulation of Kirchoff's diffraction formula with Dirichlet green's function (i.e., one that vanishes on the boundary surface). A one-dimensional Fresnel diffraction formula is used to estimate diffracted field from the observed sample and the background. The mathematical model further takes into account

the incoherent nature of the illumination source by averaging over the wavelengths of the light source. The remaining unknown parameters of the experiments are treated as free parameters and are determined by a comparison to the experimental data. Detailed explanation about diffraction theory and the mathematical model are discussed in Chapter - 2.

Experimental data used here for comparison are taken from the Master's thesis of Cardenas [9] and briefly summarized here. The thermoreflectance technique was used to measure temperature and determine thermal contact resistance for gold thin film structures used as model electrical interconnects [8, 9]. The observed sample consists of the gold thin film interconnects as seen in Fig. 1.1.



The test interconnect consists of two gold pads, thin film leads and a narrow test line connecting the two leads [23, 24]. The gold film is deposited on an amorphous SiO<sub>2</sub> substrate grown on a silicon wafer. There is thin adhesion layer of titanium between gold and SiO<sub>2</sub>. This

technique was extended to analyzing thermoreflectance data from 150 nm wide carbon nanofibers (CNFs) undergoing current stressing [25].

The thermoreflectance experiment was performed in two stages: *i*) Calibration: to obtain the thermoreflectance coefficient the entire sample was uniformly heated using a heater and the normal reflectance intensity was measured by using a microscope and CCD; and *ii*) Temperature Measurement: the TR coefficient was then used to measure temperature distribution of the thin gold structure undergoing Joule heating. In prior experiments, the calibrated TR coefficient shows good experiment with the work of Beran [26]. However, the calibrated TR coefficients under the illumination wavelengths of 470 and 530 nm yielding different values [8]. Whereas a temperature measurement from Joule heating was possible at 530 nm, the 470 nm data for the small interconnect lines were strongly influenced by diffraction. In both cases, but more pronounced at 470 nm, the size of the measurement sample affects the quality of the result. The combined effects of vibration and diffraction cause spatial averaging and convolution (blurring) and lead to mixing of the reflectance intensity of the gold film and substrate. The amount of diffraction depends upon the wavelength, the size of the sample, and the interaction with background. When measuring on the gold pads (10  $\mu\text{m}$  wide) the thermal profiles obtained from the experiment for the wavelengths 470 and 530 nm match. The disagreement in the calibration and the measurement signal exists over the narrow interconnect (1  $\mu\text{m}$  wide) samples motivates the development of a diffraction based model. We are not aware of any previous work that has investigated methods to use thermoreflectance on very narrow lines where diffraction has taken place.

The present work develops a model to characterize the diffraction, based on the size of the sample, the wavelength of the illumination, the phase shift of the signal from the background, strength of the reflectance, and the apparent distance of the image. From fitting the model with the experimental data the unknown parameters of the experiments are quantified. The parameters are optical distance between the specimen and the CCD, and the phase shift between the signals resulting from the difference in the thickness of the gold line and the substrate. Results are discussed in detail in Chapter-3 of thesis.

## **2. MATHEMATICAL MODEL**

### **2.1 Diffraction Theory:**

Diffraction is defined by Sommerfeld as any deviation of light from rectilinear path that cannot be interpreted as reflection or refraction [27]. But before that there is fascinating history associated with the discovery and explanation of diffraction effect. The first accurate description of this phenomenon was given by Grimaldi in 1665 in his book. Then in 1678 Huygens expressed the principle that if each point on the wavefront of disturbance were considered to be a new source of a “secondary” spherical disturbance, then the wavefront at a later instant could be found by constructing the “envelope” of the secondary wavelets. Then there was no significant progress on further understanding this phenomenon during 18<sup>th</sup> century. In 1804, Young introduced the concept of “interference” and there by strengthened the wave theory of light. In 1818, Fresnel first time calculated distribution of light in diffraction patterns by combining Huygens and Young’s explanation and making some arbitrary assumptions. After the Maxwell’s discovery of light as an electromagnetic wave in 1860, in 1882 the ideas of Huygens and Fresnel were put on a firmer mathematical formulation by Kirchhoff, who successfully showed that phase and amplitudes described for secondary wavelet by Fresnel is indeed logical sequence of wave nature of light. However two main assumption on boundary conditions made by Kirchhoff was later proved inconsistent by Poincare in 1892 and Sommerfeld in 1894. And therefore the Kirchhoff’s theory is known as first approximation of diffraction theory. The Kirchhoff’s theory then modified by Sommerfeld by eliminating one of the inconsistent assumption regarding the light amplitude at the boundary. Rayleigh Sommerfeld used theory of Green’s Function. In the development of the mathematical model for the thermoreflectance data Rayleigh-Sommerfeld theory is used.

The basic diffraction problem requires finding a solution to the Helmholtz equation for propagating wave encountering partial obscuring planar screen [27, 28]. The Helmholtz equation is

$$(\nabla^2 + k^2)E(\mathbf{r}) = 0 \quad (1)$$

where  $k = 2\pi/\lambda$ , the wave number and  $E$  is scalar field.

The boundary condition imposed on the solution to this differential equation is the effect of a diffracting screen in the  $z = 0$  plane (Fig. 2.1).

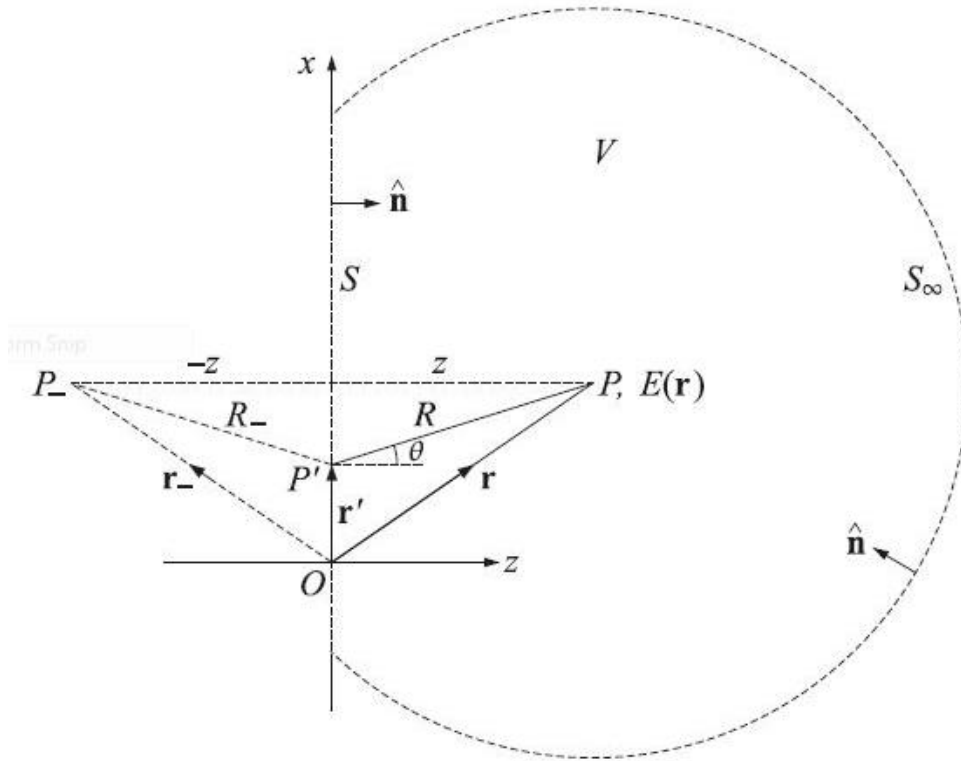


**Fig. 2.1: Diffraction field for Rayleigh-Sommerfeld diffraction Integral**

The Rayleigh-Sommerfeld diffraction integral is given as [29]:

$$E(\mathbf{r}) \iint = 2 \iint_S E(\mathbf{r}_0) \frac{\partial G}{\partial z} dS \quad (2)$$

where G is the Green's function for the Helmholtz equation.

$$G(r - r_0) = \frac{e^{-jk|r-r_0|}}{4\pi|r-r_0|} \quad \text{or} \quad G(r_{01}) = \frac{e^{-jkR}}{4\pi R} \quad \text{and} \quad (3)$$

$$\left. \frac{\partial G}{\partial z} \right|_{z=0} = \frac{z}{R} \left( jk + \frac{1}{R} \right) \frac{e^{-jkR}}{4\pi R} \quad (4)$$

Substituting value of indicated derivative in equation (2)

$$E(r) = \iint_S E(r_0) \frac{2z}{R} \left( jk + \frac{1}{R} \right) \frac{e^{-jkR}}{4\pi R} dS \quad (5)$$

$$\text{In this equation } R = |r - r_0| = \sqrt{(x - x_0)^2 + (y - y_0)^2 + z^2} \quad (6)$$

Now if we assume that diffracting aperture has dimension 'a' so that  $x_0^2 + y_0^2 \ll a^2$  and further if we assume that z is large enough that Fresnel number ( $N_f$ ) =  $\frac{a^2}{\lambda z}$  is small enough then equation (5) simplifies to

$$E(x, y, z) = \frac{jk}{2\pi z} e^{-jkz} \iint E(x_0, y_0, 0) e^{-jk|(x-x_0)+(y-y_0)|^2/2z} dx_0 dy_0 \quad (7)$$

The above mentioned approximation is called Fresnel approximation.

In the special case when the aperture field  $E(x_0, y_0, 0)$  depends only one transverse coordinate, say,  $E(x_0, 0)$  the dependence of equation (7) on the y direction can be integrated out using the integral

$$\sqrt{\frac{jk}{2\pi z}} \int_{-\infty}^{\infty} e^{-jk(y-y_0)^2/2z} dy_0 = 1 \quad (8)$$

and we obtain the following one-dimensional Fresnel formula:

$$E(x, z) = \sqrt{\frac{jk}{2\pi z}} e^{-jkz} \int_{-\infty}^{\infty} E(x_0, 0) e^{-jk(x-x_0)^2/2z} dx_0 \quad (9)$$

## 2.2 Diffraction by Single slit:

The incident field is uniform plane wave,  $E_{inc}(x, z) = E_0 \exp(-jkz)$ , whose value on slit is  $(x_0, 0) = E_0$ .

The diffracted field at distance 'z' from equation (9)

$$E(x, z) = \frac{\sqrt{jk}}{2\pi z} e^{-jkz} \int_{-\infty}^{\infty} E(x_0, 0) \exp\left(-\frac{jk(x-x_0)^2}{2z}\right) dx_0$$

$$= E_0 \frac{\sqrt{jk}}{2\pi z} e^{-jkz} \int_{-a}^a \exp\left(-\frac{jk(x-x_0)^2}{2z}\right) dx_0 \quad (10)$$

where 'a' is the half-width of the slit. The integral can be reduced to Fresnel Integral by changing variable as follows:

$$\sqrt{\frac{k}{2z}}(x-x_0) = \sqrt{\frac{\pi}{2}}u \quad \& \quad v_{\pm} = \sqrt{\frac{k}{\pi z}}(\pm a - x) \quad (11)$$

With this substitution equation (10) reduces to

$$\frac{\sqrt{jk}}{2\pi z} \int_{-a}^a \exp\left(-\frac{jk(x-x_0)^2}{2z}\right) dx_0 = \sqrt{\frac{j}{2}} \int_{v_-}^{v_+} \exp\left(-\frac{j\pi u^2}{2}\right) du$$

$$= \frac{F(v_+) - F(v_-)}{1-j} \quad (12)$$

Thus  $E(x, z) = \exp(-jkz) D(x, z)$ ,

where,

$$D = \frac{F(v_+) - F(v_-)}{1 - j} \quad (13)$$

$$\text{Intensity } (I) = E \times E^* \quad (14)$$

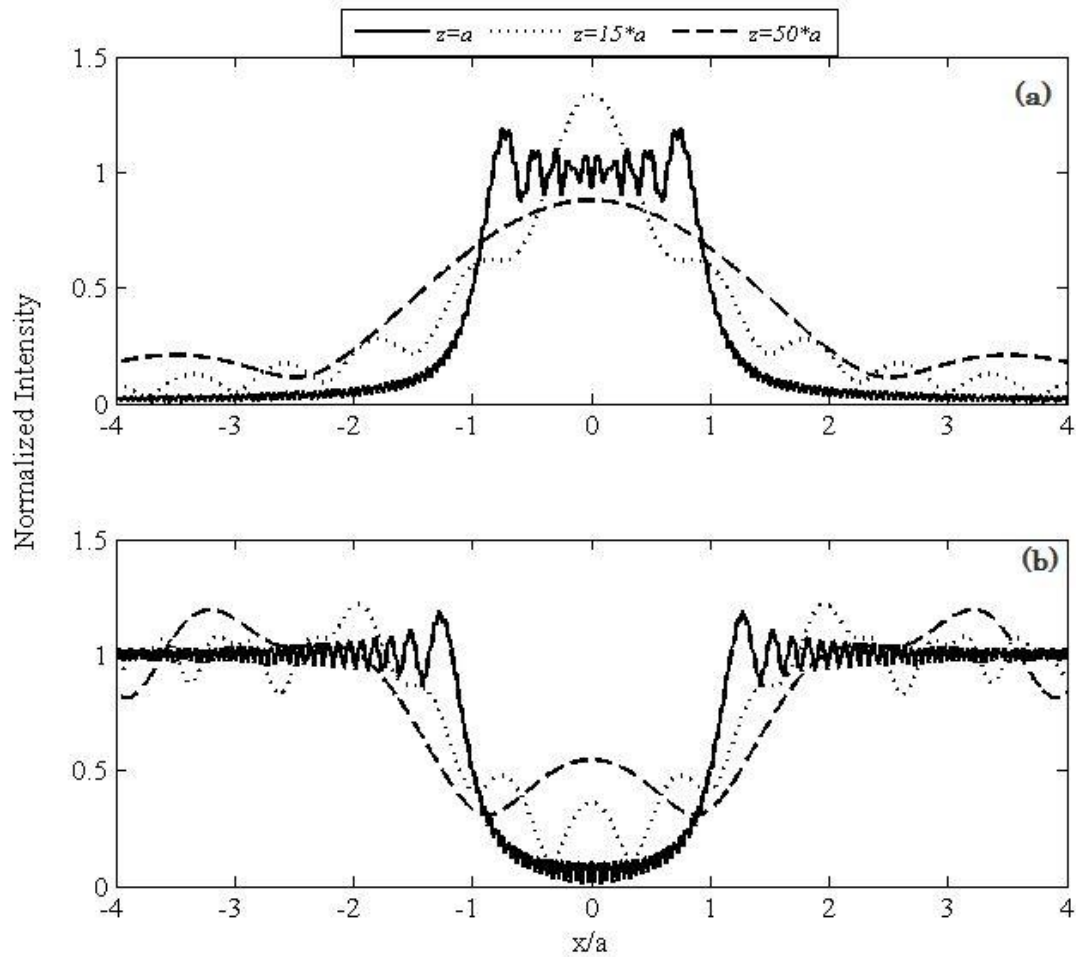


**Figure 2.2 Effect of distance  $z$  on diffracted field intensity (a) slit (b) strip for different image plane distances from the sample**

The normalized intensity for the slit at different ' $z$ ' values are plotted in Fig. 2.2 (a). As we can see from plot the effect of diffraction is more profound in the near field i.e. when  $z = a$ . The effect of diffraction is very blur in the far filed region when  $z = 100*a$ .

### 2.3 Diffraction by Strip:

For the case of strip limits of integration are changed

$$\begin{aligned} & \sqrt{\frac{jk}{2\pi z}} \left( \int_a^\infty + \int_{-\infty}^{-a} \right) \exp\left(-\frac{jk(x-x_0)^2}{2z}\right) dx_0 \\ &= \frac{F(\infty) - F(v_+) + F(v_-) - F(-\infty)}{1-j} = 1 - D(x, z) \end{aligned} \quad (15)$$

Where we used  $F(\infty) = -F(-\infty) = (1-j)/2$

Thus, the diffracted field in case of strip

$$E(x, z) = \exp(-jk/z)[1 - D(x, z)] \quad (16)$$

$$\text{Intensity } (I) = E \times E^* \quad (17)$$

The normalized intensity for the strip is plotted in Fig 2.2 (b) for different values of ‘z’

## 2.4 Mathematical Model:

The total reflected intensity imaged by CCD is coming from two different surfaces with different reflectivity, the gold film and substrate. Accordingly, the mathematical model consists of two parts (Fig 2.3): the reflectance intensity coming from the metallic gold film and the reflectance intensity coming from the background substrate. The two intensities are combined to yield the total reflected intensity. Light coming from the gold film is treated as diffraction through a slit due to the high reflectivity of gold. In the latter case, the reflected light coming from the substrate is obstructed by gold thin film on its way to the microscope. Hence the reflection coming from the substrate is treated as diffraction past a strip.

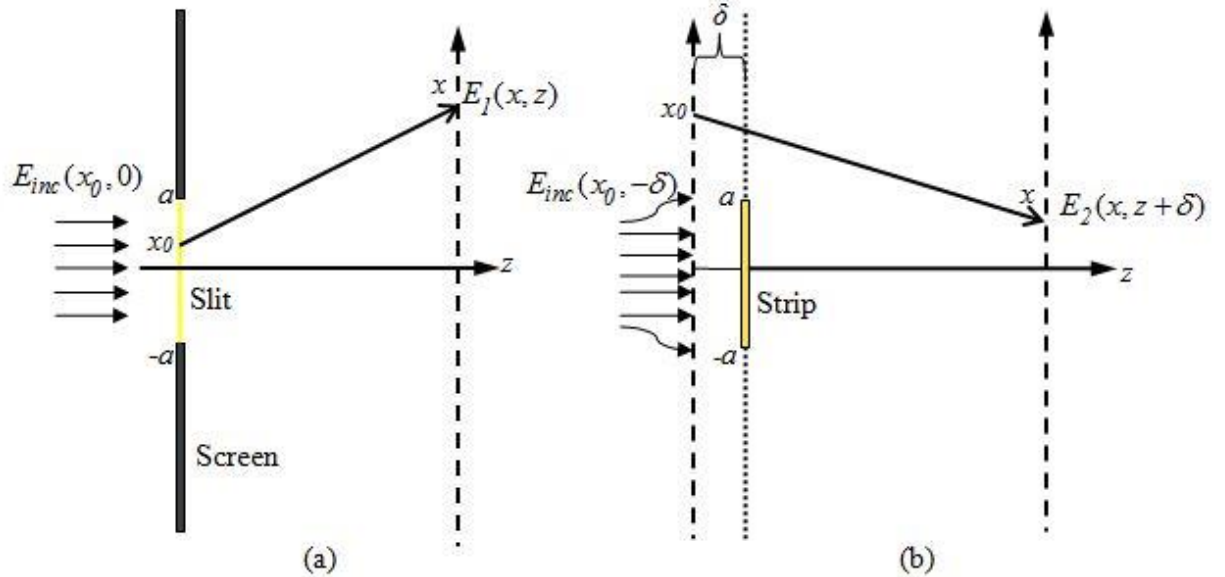


**Figure 2.3 Mathematical model set-up composed of reflection from the sample and substrate based on two simple diffraction model (a) The diffracted field for the gold line, where gold line is treated as slit (b) The diffracted field for the substrate, where gold line is treated as a strip blocking the light reflected from the substrate.**

For the first part Eq. 13-14 is used while for the second part Eq. 16-17 needs to be modified to take into account the difference in the distance traveled by the light before coming to CCD. The signal coming from the substrate is travelling a longer distance  $2 \cdot \delta$  as compared to the signal originating from the gold line which results in a phase shift between the two signals. The longer distance travelled accounts for the transparent silicon-dioxide layer between the gold film and the reflective silicon substrate.

In the case of the strip,

$$E_2(x, z + 2\delta) = \exp(-j(kz - \varphi)) \left[ \frac{F(\infty) - F(v_+) + F(v_-) - F(-\infty)}{1 - j} \right] \quad (18)$$

The total diffracted field can be obtained as

$$E_{total} = E_1 + \Gamma \cdot E_2 \quad (19)$$

where  $\Gamma$  is the ratio of the reflectivity of gold and the substrate material.

Then the total reflected intensity

$$I_{total} = E_{total} \cdot E_{total}^* \quad (20)$$

In the experiment the intensity measured by CCD is in arbitrary units. The model quantified total intensity in physical units. To compare the model with the experimental data, the total reflected intensity obtained from model is multiplied by the gain factor  $\gamma$

$$I_{model} = \gamma I_{total} \quad (21)$$

### 3. RESULTS & ANALYSIS

The two-dimensional Joule-heating data for the sample were taken using the experimental setup for the wavelengths of 470 and 530 nm. For a single wavelength, the results are repeatable for increasing and decreasing current; however, for the same sample the temperature distribution under two different LED wavelengths resulted in inconsistency.

In calculations the following two unknowns in the experiment are considered as fitting parameters: optical distance  $z$ , the distance between the observed specimen and the imaged plane, and phase shift  $\varphi$ , the shift in phase between the signal coming from the gold line and the substrate. The optical distance is dependent on the overall imaging of the microscope and is treated as a fitting parameter. The phase shift is dependent on the thickness of the oxide layer which is an increase in path length for the light to travel before reflecting off the silicon substrate. While treated as a fitting parameter, the phase shift must fall within a range consistent with this added path length. The effect of different  $z$  values is shown on each of the two components, in chapter-2 Fig. 2.2(a) for the slit  $a = 4\lambda$  and Fig. 2b for the same size strip. As can be seen from these figures the effect of diffraction is profound in the near field when  $z = a$ , whereas it is more blurred for the far field when  $z = 50a$ . The Fresnel number ( $F = a^2/\lambda z$ ) in our cases spans the range 0.1 to 3.5 which is on the order of 1. The Fraunhofer approximation is the limiting case when the optical distance  $z$  is large and  $F \ll 1$ . The Fresnel approximation is a partial series solution that is accurate in the limit  $F \gg 1$ , but can also be applied in the range  $F \sim 1$  with lower accuracy due to the truncated terms in the series [27, 29]. For a consistent approach we have used the Fresnel calculation. The optical distance  $z$  is an unknown in the experiment and is used as a fitting parameter when the model is compared to the data.

To fit the model parameters with experimental data least squares minimization is used to determine the best values for  $z$  and  $\varphi$ , starting from initial estimates of their values. This procedure is implemented in MATLAB. Since the experimental data are given in terms of averages of images from a CCD camera the least squares procedure also normalizes the absolute image strength with a gain parameter and accounts for the

difference in reflectivity of the gold and the silicon substrate which is consistent with published reflectivity for the two materials.

The other two fitting parameters, reflectance ratio  $\Gamma$  and gain parameter  $\gamma$ , are for normalizing the overall intensity in the model with experimental data. The total reflectance intensity comes from two different surfaces, gold line and substrate, with different reflectivities. Further, to consider the optical absorption and the intensity of light source, the two diffracted field intensities are combined in the model with the help of the reflectance ratio  $\Gamma$ . The values of the material's reflectivity at ambient temperature of 25 °C depend upon the wavelength and are available in literature [30]. The last fitting parameter is  $\gamma$  a gain parameter that converts the normalized intensity signal to the range on the CCD.

During the experiment the combined effects of vibration and noise smooth out the data, and result in an intensity profile that lacks small scale intensity signal variation seen in the model. This real filtering is due to the integration over the CCD pixels, physical vibration in the system, and diffraction in the optics. Therefore some additional spatial average is applied to the model data. The spatial average is performed by calculating moving average over a window of 11 pixels where each pixel is 0.0539  $\mu\text{m}$  in width. As the LEDs used in the experiment are not monochromatic the diffracted field and hence the reflectance intensity calculated with the mathematical model is integrated over the spectral width and strength of the LEDs. An attempt was made to take into account the incoherent nature of LEDs by performing phase average. Accounting for this wavelength variation did not significantly changes the nature of the intensity profile.

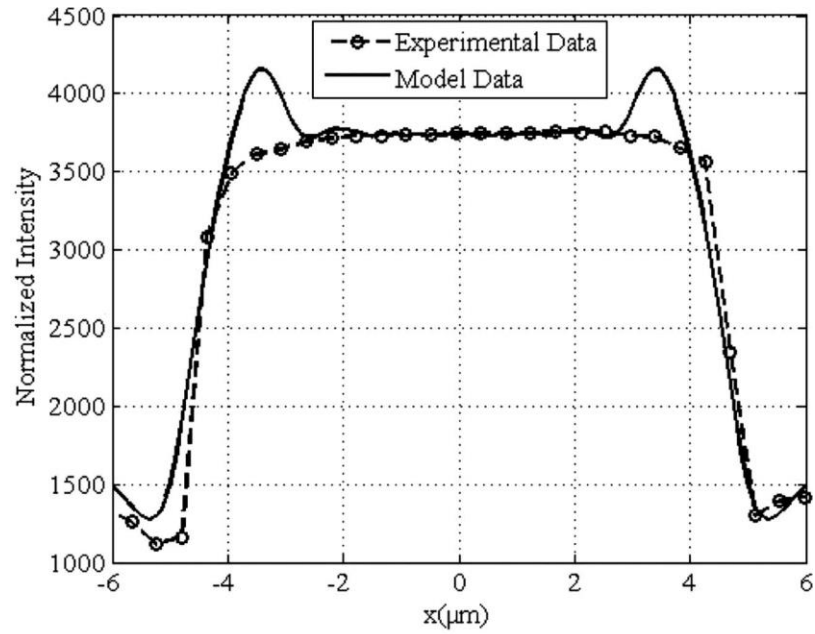
In Fig. 3.1. The model is compared with the experimental data at the wide section for wavelength of 535 nm. The parameters used to generate this figures are summarized in Table 3.1. Although not an exact match, the model shows very good qualitative agreement with the experimental data. At the edge of the gold line the model both underestimate and overestimates, the intensity. This is caused mainly by the edge diffraction effect and limited experimental data available for the substrate signal. This small scale oscillatory behavior is smoothed in the experimental data because of

averaging in the CCD, vibration in the system, variation in the coherence of the light, and diffraction due to thermal gradient in the air above the sample.

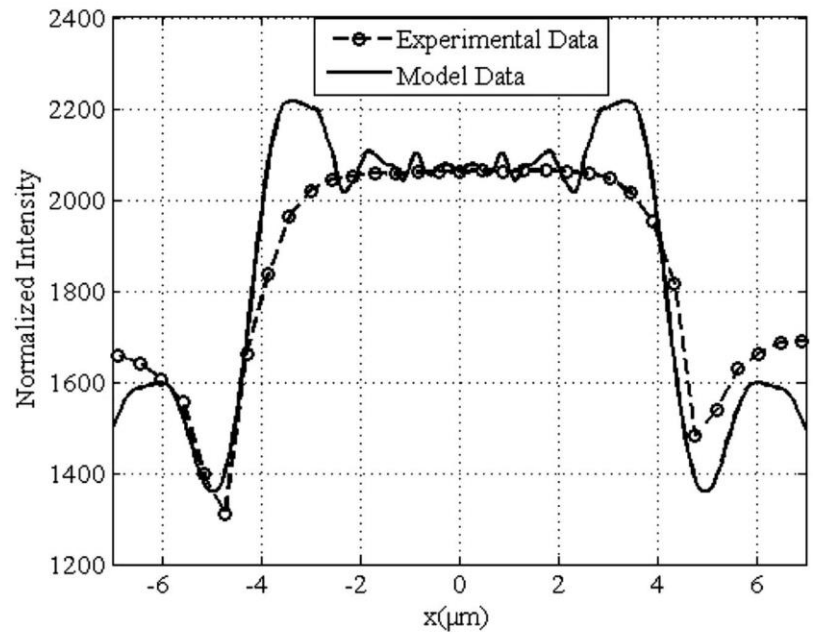
In Fig. 3.1b the model data are compared with the experimental data at the same wide section but for a different illumination wavelength, 470 nm. Similar matching of the model and the experiment is observed. As the wavelength of illumination changes the reflectance, optical distance and phase shift should change. The new values of these parameters for the fitting is obtained from the algorithm confirmed the theoretical values. The values are summarized in Table 1.

**Table 3.1: Summary of Fitting parameters**

Wavelength (nm)	$a$ ( $\mu\text{m}$ )	$z$ ( $\mu\text{m}$ )	$\phi$ (rad)	$r$	$\gamma$
535	5	20	2.2	0.64	3700
	0.5	3.75	2.2	0.64	3400
470	5	15	2.12	0.9	2068
	0.5	5.75	2.12	0.9	1068



(a)



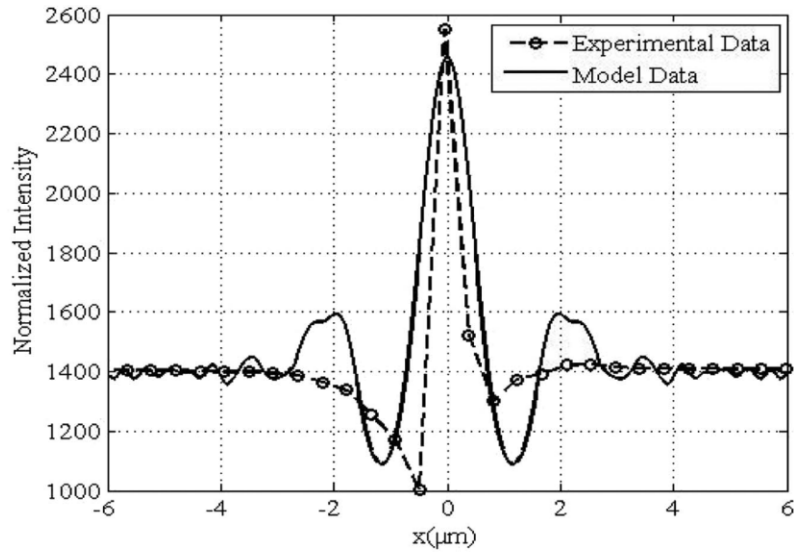
(b)

**Fig. 3.1** Plot of experimental data and model for 10  $\mu\text{m}$  wide gold interconnect for (a.)  $\lambda = 535\text{ nm}$  at section a-a of Fig. 1.1 (c) and (b.)  $\lambda = 470\text{ nm}$  at section a-a of Fi. 1.1 (c)

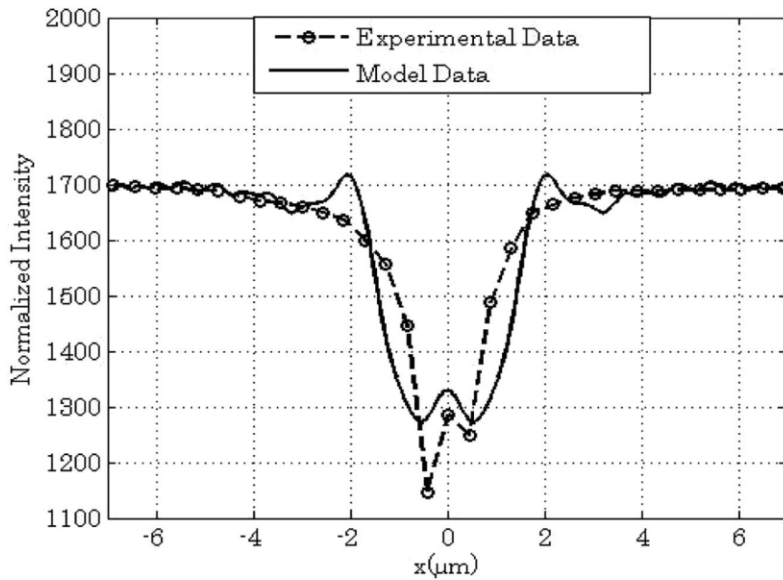
Fig. 3.2 (a) shows the fit for the narrow-field at wavelength of 530 nm. When moving from wide-section to narrow section for the same wavelength the optical distance should change and as result the phase shift. The values of these two parameters are varied

to fit the model data to the experimental data. As can be seen the model data fits with the experimental data except at the edge; again the model overestimates the experiment peaks.

Fig. 3.2 (b) shows the comparison of model and experimental data at narrow-section for the wavelength of 470 nm. The overall reflectivity of gold at 470 and 530nm is very different, around 0.4 to 0.6 and combined with the temperature dependence of the reflectivity, the diffraction patterns of both wavelengths along the gold line are different. By varying the optical distance  $z$  same amount as done for 530 nm the model doesn't provide a good fit with the experimental data. Different values of  $z$  were tested and the values listed in Table 2 give qualitative good fit for the data.



(a)



(b)

**Fig. 3.2 Plot of experimental data and model for 1  $\mu\text{m}$  wide gold interconnect for (a)  $\lambda$  \_ 535 nm at Section b-b of Fig. 1.1(c) and (b)  $\lambda$  \_ 470 nm at Section b-b of Fig. 1.1(c).**

The use of thermoreflectance for temperature measurement has been well established based on its ability to generate a full field measurement, but there is an increasing desire to apply this technique to smaller spatial scales. As a result there is a need to understand the impact of optical limits on the signal generated. This is the first known work applying a diffraction model to understand the thermoreflectance signal and it will be useful in extending the technique to smaller

scales. The diffraction model considers the reflection signal produced from samples of thin films on and from the substrate.

Four parameters are used in the model for fitting with experimental data. The results show good agreement between calculated and measured values. The overall reflectivity of gold at 470 and 530 nm changes significantly from 0.4 to 0.6 and this change is captured by the model. The diffraction patterns for 470 and 530 nm produce different data profiles. Furthermore, the thermoreflectance signal at each wavelength over the narrow line, one micron is significantly different than the wide-field due to the impact of the diffraction.

#### 4. Conclusions & Future work

The use of thermoreflectance for temperature measurement has been well established based on its ability to generate a full field measurement, but there is continuous demand to improve the spatial resolution to keep up the pace with the size of current optoelectronic and electronic devices. As the spatial resolution is limited by onset of optical diffraction, it is necessary to better understand the limit imposed by diffraction and propose solutions to overcome this barrier. This is the first work applying a diffraction model to understand the thermoreflectance signal. In most of electronic and optoelectronic applications thin metal film is protected by dielectric layer. The reflectance signals coming from the metal film is interfered by the diffused signal coming from the dielectric substrate. Due to this interference, the calibration procedure or in other words to find the thermoreflectance coefficient for the given metal is very complex experimental methodology. In current work model is developed considering the optical interference coming from dielectric - substrate layer along with the reflectance coming from the thin metal film.

Four parameters are used in the model for fitting with experimental data. The results show good agreement between results calculated using the developed model and experimental data. The overall reflectivity of gold at 470 nm and 530 nm changes significantly from 0.4 to 0.6, and this change in reflectivity is reproduced in model calculated values. During the experiment the temperature profile mapped with illumination wavelength of 470 and 530 nm are quite different. As well as, the diffraction pattern for each wavelength is significantly different for the narrow (1  $\mu\text{m}$  wide) line as compared to the wider (10  $\mu\text{m}$  wide) line. All these experimental observations are well captured by the model. This model will help to improve the spatial resolution of the thermoreflectance method and further will lead to simplify the calibration method in the given spectral range of illumination wavelength.

When this work is done thermoreflectance method is limited to the visible range of wavelength. The model is developed considering the two illumination wavelengths only. This work can be further extent to the other wavelength in the visible range and even to go for nanometers spatial resolution UV range. This model is developed for gold thin film on based of theory of diffraction by slit and strip. In future to understand the thermoreflectance signals coming from Carbon Nano Fibers (CNFs), nanorods and nanodots model can be extent with diffraction by circular aperture.

## REFERENCES

1. International Technology Roadmap for Semiconductors, 2013, available at <http://www.itrs.net/Links/2013ITRS/2013Chapters/2013Interconnect.pdf>
2. O. Nakabeppu, and T. Suzuki, "Microscale temperature measurement by scanning thermal microscopy", *J. Therm. Anal. Calorim.* **69**, 727-737 (2002).
3. D. Cahill, K. Goodson, and A. Majumdar, "Thermometry and thermal transport in micro/nanoscale solid-state devices and structures" *J. Heat Transfer*, **124** 223-241 (2002).
4. J. Christofferson, K. Maize, Y. Ezzahri, J. Shabani, X. Wang, and A. Shakouri, "Microscale and nanoscale thermal characterization techniques," in *Thermal Issues in Emerging Technologies*, Cairo, Egypt, 2007, pp. 3–9.
5. L. Wenjun, and B. Yang, "Thermography techniques for integrated circuits and semiconductor devices." *Sensor Review* 27, no. 4 (2007): 298-309.
6. M. Farzaneh, K. Maize, D. Lüerßen, J. A. Summers, P. M. Mayer, P. E. Raad, K. P. Pipe, A. Shakouri, R. J. Ram, and Janice A. Hudgings. "CCD-based thermoreflectance microscopy: principles and applications." *Journal of Physics D: Applied Physics* 42, no. 14 (2009): 143001.
7. J. Christofferson, and A. Shakouri "Thermoreflectance based thermal microscope" *Rev. Sci. Instrum.* **76** 1-6 (2005).
8. C. Cardenas, D. Fabris, S. Tokairin, F. Madriz, and C. Y. Yang, "Thermoreflectance measurement of temperature and thermal resistance of thin film gold", *J. Heat Transfer*, **134**, No. 11, (November, 2012).
9. C. Cardenas, "Thermoreflectance Temperature Measurement and Application to Gold Thin Films and Carbon Nanofibers" M.S. Thesis, Dept. of Mechanical Engineering, Santa Clara University, (2011).
10. G. Tessier, S. Holé, and D. Fournier, "Quantitative Thermal Imaging by Synchronous Thermoreflectance with Optimized Illumination Wavelengths," *Applied Physics Letters*, 2001, doi:10.1063/1.1363696.

11. G. Tessier et al., "Measuring and Predicting the Thermoreflectance Sensitivity as a Function of Wavelength on Encapsulated Materials," in *Review of Scientific Instruments*, 2003, doi:10.1063/1.1517153.
12. G Tessier et al., "Thermoreflectance Temperature Imaging of Integrated Circuits: Calibration Technique and Quantitative Comparison with Integrated Sensors and Simulations," *J. Phys. D: Appl. Phys* **39** (2006): 4159–66, doi:10.1088/0022-3727/39/19/007.
13. T. Favalaro, , J-H. Bahk, and A. Shakouri. "Characterization of the temperature dependence of the thermoreflectance coefficient for conductive thin films." *Review of Scientific Instruments* 86, no. **2** (2015): 024903.
14. P. L. Komarov, M. G. Burzo, and P. E. Raad, "CCD thermoreflectance thermography system: Methodology and experimental validation" *THERMINIC 12*, Nice, France, 2006.
15. K. Maize, J. Christofferson, and A. Shakouri, "Transient thermal imaging using thermoreflectance." In *Semiconductor Thermal Measurement and Management Symposium*, 2008. *Semi-Therm 2008*. Twenty-fourth Annual IEEE, pp. 55-58. IEEE, 2008.
16. K. Yazawa, D. Kending, D. Hernandez, K. Maize, and A. Shakouri, "Challenges and opportunities for transient thermal imaging of microelectronic devices", *Thermal Investigations of ICs and Systems (THERMINIC)*, 2012 18th International Workshop on, **1, 4**, 25-27 (Sept. 2012).
17. A. J. Schmidt, R. Cheaito, and M. Chiesa, "Characterization of Thin Metal Films via Frequency-Domain Thermoreflectance," *Journal of Applied Physics*, 2010, doi:10.1063/1.3289907.
18. D. Kim et al., "Quantitative Thermal Characterization of Microelectronic Devices by Using CCD-Based Thermoreflectance Microscopy," doi:10.1117/12.2041052.
19. K. Maize et al., "Thermoreflectance CCD Imaging of Self-Heating in Power MOSFET Arrays," *IEEE TRANSACTIONS ON ELECTRON DEVICES* 61, no. **9** (2014), doi:10.1109/TED.2014.2332466.

20. S. Grauby, A. Salhi, L. P. Lopez, W. Claeys, B. Charlot, S. Dilhaire, "Comparison of thermorefectance and scanning thermal microscopy for microelectronic device temperature variation imaging: Calibration and resolution issues", *Microelectronics Reliability* **48**, 204-211 (2008).
21. Ziabari *et al.*, "Sub-diffraction limit thermal imaging for HEMT devices," *Thermal Measurement, Modeling & Management Symposium (SEMI-THERM), 2015 31st*, San Jose, CA, 2015, pp. 82-87.
22. J. W. Goodman, "Introduction to Fourier Optics", 3<sup>rd</sup> Edition, Roberts and Company, (2005).
23. F. R. Madriz, J. R. Jameson, S. Krishnan, X. Sun, and C. Y. Yang, "Circuit modeling of high-frequency electrical conduction in carbon nanofibers", *IEEE transactions on electron devices.*, **56**, **8**, ( August 2009).
24. F. R. Madriz, J. R. Jameson, S. Krishnan, X. Sun, and C. Y. Yang, "Test structure to extract circuit model of nanostructures operating at high-frequencies", in *IEEE Int. Conf. Microelectron. Test Struct.*, 138-40 (March 2009).
25. S. Tokairin, K. Read, P. Wilhite, J. Chen, D. Fabris, and C. Y. Yang, "Thermorefectance of carbon nanofibers: Joule Heating experiment and calibration", 10<sup>th</sup> International Conference on Heat Transfer, Fluid Mechanics and Thermodynamics, Orlando, Florida, (14 – 16 July 2014).
26. Beran, "The reflectance behavior of gold at temperatures up to 500 °C" *TMPM Tschermaks Mineralogische und Petrographische Mitteilungen*, **34**, 11-215 (1985).
27. F. L. Pedrotti, L. M. Pedrotti and L. S. Pedrotti, "Introduction to Optics", 3<sup>rd</sup> Edition, Addison-Wesley, (2006).
28. M. Born and E. Wolf, "Principles of Optics", 7th Edition, (1999).
29. S. J. Orfanidis, *Electromagnetic Waves and Antennas*, available online at [www.ece.rutgers.edu/~orfanidi/ewa](http://www.ece.rutgers.edu/~orfanidi/ewa) (2008).
30. E. Palik, "Handbook of Optical Constants of Solids", Elsevier, (1998).

## APPENDICES:

### A.1 Experimental Details:

The experimental setup to perform normal reflectance intensity analysis as a function of sample temperature is shown in Fig. A.1. It consists of an LED illumination source, CCD, optical microscope, sample holder and acquisition equipment. A modified Meiji Techno microscope Series MC-50T is used as the central component of the system. A beam splitter is placed at the core of the microscope to guide collimated incident rays and an aperture constrains the illumination beam onto the surface of the samples. Reflected light is transferred through the beam splitter to the CCD. A 12-bit A/D Prosilica GE1380 CCD camera is used to capture the reflectance intensity images. Illumination is generated from Luxeon® Star/O series LEDs. The spectral characteristics, as mentioned by manufacturer, of the two LEDs used in this research is enlisted in Table A.1. A custom designed heater microscopy stage assembly is used to support samples while providing thermal control over a temperature range from ambient 20 to 250 °C [8].

**Table A.1. Spectral characteristics of LEDs**

Color	$\lambda_{\min}$ (nm)	$\lambda_{\text{peak}}$ (nm)	$\lambda_{\max}$ (nm)	Spectral Half Width $\Delta \lambda_{1/2}$ (nm)
Blue	460	470	490	25
Green	520	530	550	35

The TR calibration coefficient  $\kappa$  is acquired prior to performing the measurements. Calibrations were performed for the two LEDs of central wavelengths 470 and 535 nm. Measurements of the sample temperature,  $T$ , and the normal reflectance intensity  $I_n(T)$  over sufficiently large regions of the material were used to compute  $\kappa$ . Under LED illumination with a peak wavelength of 535 nm, the average value of the calibration coefficient was  $-1.71 \times 10^{-4} \text{ } ^\circ\text{C}^{-1}$  with a standard deviation of  $0.19 \times 10^{-4} \text{ } ^\circ\text{C}^{-1}$ . Under LED illumination with 470 nm, the average value of the calibration

coefficient was  $1.76 \times 10^{-4} \text{ } ^\circ\text{C}^{-1}$  with a standard deviation of  $2.1 \times 10^{-5} \text{ } ^\circ\text{C}^{-1}$ . These values demonstrate good agreement with the previous results of Beran for gold [26].

The second mode of the experiment is to acquire two-dimensional TR images of the calibrated structure during Joule heating. During this mode of operation, a function generator, amplification circuitry and a delay generator are used to create a delay locked loop tuned to acquire images of the periodically heated sample during the quasi-steady heating and relaxation regimes. A reflectance intensity image of the sample acquired under illumination at  $\lambda_{\text{peak}} = 530 \text{ nm}$  is shown in Fig. 1c. Following the acquisition of the heated and relaxed state images, processing was done for the computation of the temperature difference using TR coefficient and Eq. 2 and 3. During Joule heating experiments adequate manual correction of positioning with superposition of a reference image and a focal metric calculation are performed to correct for displacements due to the thermal expansion. The thermal expansion of the system is estimated to be 0.3% and does not result in a significant change in system size relative to the wavelengths considered. Due to high optical absorption of gold in the visible range it was assumed during experiment that the surface reflection is dominant and the film is sufficiently thick to be considered optically opaque. At 100 nm the film thickness is 4.6 times the material's absorption coefficient which governs the exponential decay of the electromagnetic wave in the gold. TR response has been shown to be linear over the calibration temperature range of 20-200  $^\circ\text{C}$ .

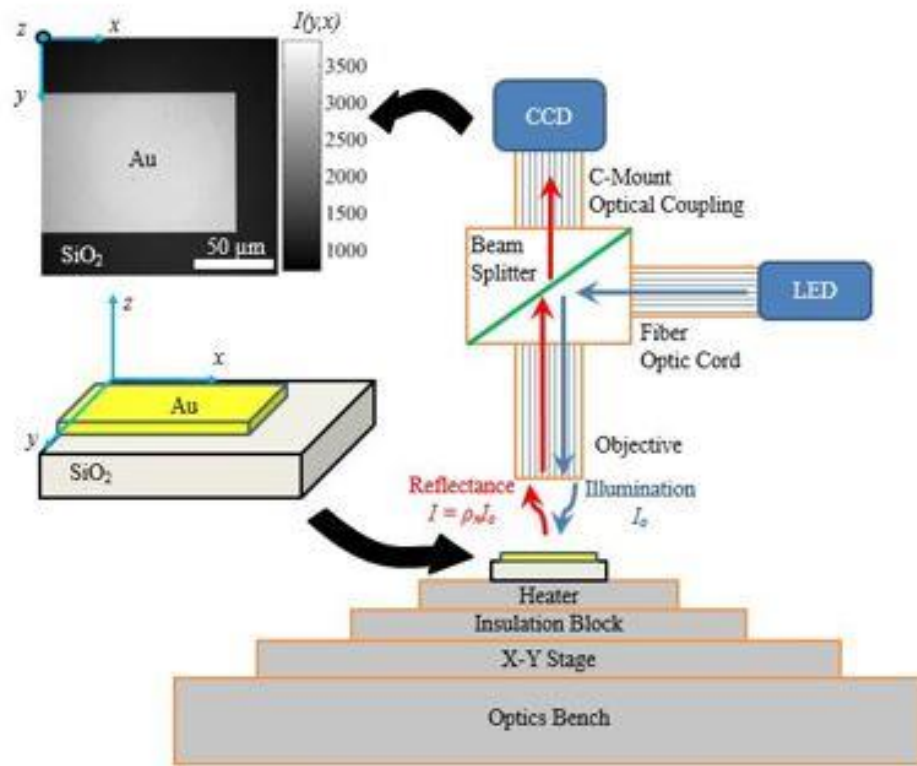


**Fig. A.1 Schematic of Thermoreflectance temperature measurement experimental set-up**

## A.2 MATLAB Code

### 1. To generate the figure:

```

I_530=figure_1(0.530,5,20,0.64,3700,(3*pi)/4);
I_470=figure_470(0.470,4.73,5,0.9,555,2.22);
load 530Rows
I_Exp_1=avgrW(:,1);
subplot(2,1,1);
plot(xs(1:8:end),I_Exp_1(1:8:end),'k--o',xs,I_530,'k-','LineWidth',2);
line1=get(gca,'Children');
set(gca,'FontSize',12,'FontName','Times New Roman')

hold on
%%plot(xs(1:10:end),I_Exp(1:10:end),'k-
o','LineWidth',2);set(gca,'FontSize',12,'FontName','Times New Roman')

set(findall(gcf,'type','text'),'FontSize',12,'FontName','Times New
Roman')
%%xlabel('x(μm)');
ylabel('Intensity(A.U.)');
xlim([-8,8]);
%%title('Comparison of Model data and Experimental data at wide section
for wavelength lambda=530');

```

```

title('\lambda=530nm');
%%grid on
load 470Rows
I_Exp_2=avgrW(:,1);
subplot(2,1,2);
plot(xs(1:8:end),I_Exp_2(1:8:end),'k--o',xs,I_470,'k-','LineWidth',2);
line2 = get(gca,'Children');
set(gca,'FontSize',12,'FontName','Times New Roman')
set(findall(gcf,'type','text'),'FontSize',12,'FontName','Times New Roman')
xlabel('x( $\mu$ m)'); ylabel('Intensity(A.U.)');
xlim([-7,7]);
title('\lambda=470nm');
h = [line1;line2];
%legend(h,'Model data','Experimental data','location','NorthOutside')
legend('Experimental Data','Model Data');
%%grid on

```

### Functions:

```

function [ I_new ] = figure_1(lambda,a,z,c,g,p)
k=(2*pi)/lambda; N_F=(a^2)/(lambda*z);
load 530Rows % **
w=sqrt(2*N_F);
v1=w*N_F.*(1-(xs/a)); % **
v2=w*N_F.*(1+(xs/a)); % **
F1=fcs(v1);
F2=fcs(v2);
D=(F1+F2)./(1-j);% **
E1=exp(j*k*z).*D;
I1=E1.*conj(E1);
E2=exp(j*(k*z-p)).*(1-D);
I2=E2.*conj(E2);
E=E1+c.*E2;
II=E.*conj(E);
I=g.*II;
I_new=moving_average(I,13);
end

```

```

function [ I_new ] = figure_470( l,a,z,c,g,p )
k=(2*pi)/l;
load 470Rows;
w=sqrt(k/pi/z);
v1=w.*(a-xs); % **
v2=w.*(-a-xs); % **
F1=fcs(v1);
F2=fcs(v2);
D=(F1-F2)./(1-li)+(F1+(1-li)/2-F2);% **
E1=exp(-li*k*z).*D;
I1=E1.*conj(E1);
E2=c.*exp(-li*(k*z-p)).*(1-D);
I2=E2.*conj(E2);
E=E1+ E2;
II=E.*conj(E);

```

```

I=(g.* II);
I_new=moving_average(I,13);

end

```

### Fraunhofer diffraction code:

```

function F = fcs(x)

if nargin==0, help fcs; return; end

F = zeros(size(x));           % defines the size of F

F = fcs2(pi*x.^2/2);

i = find(x<0);
F(i) = -F(i);                 % F(x) is an odd function

function F = fcs2(x)

if nargin==0, help fcs2; return; end

a = [ 1.595769140, -0.000001702, -6.808568854, -0.000576361,
      6.920691902, -0.016898657, ...
      -3.050485660, -0.075752419,  0.850663781, -0.025639041, -
      0.150230960,  0.034404779];

b = [-0.000000033,  4.255387524, -0.000092810, -7.780020400, -
      0.009520895,  5.075161298, ...
      -0.138341947, -1.363729124, -0.403349276,  0.702222016, -
      0.216195929,  0.019547031];

c = [ 0,
      -0.024933975,  0.000003936,  0.005770956,
      0.000689892, -0.009497136, ...
      0.011948809, -0.006748873,  0.000246420,  0.002102967, -
      0.001217930,  0.000233939];

d = [ 0.199471140,  0.000000023, -0.009351341,  0.000023006,
      0.004851466,  0.001903218, ...
      -0.017122914,  0.029064067, -0.027928955,  0.016497308, -
      0.005598515,  0.000838386];

A = fliplr(a+j*b);
C = fliplr(c+j*d);

x = abs(x);

F = zeros(size(x));

m = find(x<=4);

```

```
n = find(x>4);  
  
F(m) = exp(-j*x(m)) .* sqrt(x(m)/4) .* polyval(A, x(m)/4);  
F(n) = exp(-j*x(n)) .* sqrt(4./x(n)) .* polyval(C, 4./x(n)) + (1-j)/2;
```